

# High-dimensional spatial teleportation enabled by nonlinear optics

Bereneice Sephton,<sup>1</sup> Adam Vallés,<sup>1,2,3,\*</sup> Isaac Nape,<sup>1</sup> Mitchell A. Cox,<sup>4</sup> Fabian Steinlechner,<sup>5,6</sup>

Thomas Konrad,<sup>7,8</sup> Juan P. Torres,<sup>3,9</sup> Filippus S. Roux,<sup>10</sup> and Andrew Forbes<sup>1,†</sup>

<sup>1</sup>*School of Physics, University of the Witwatersrand, Private Bag 3, Wits 2050, South Africa*

<sup>2</sup>*Molecular Chirality Research Center, Chiba University,*

*1-33 Yayoi-cho, Inage-ku, Chiba 263-8522, Japan*

<sup>3</sup>*ICFO - Institut de Ciències Fotoniques, The Barcelona Institute of Science and Technology, Castelldefels (Barcelona) 08860, Spain*

<sup>4</sup>*School of Electrical and Information Engineering,*

*University of the Witwatersrand, Johannesburg, South Africa*

<sup>5</sup>*Fraunhofer Institute for Applied Optics and Precision Engineering, Albert-Einstein-Str. 7, 07745 Jena, Germany*

<sup>6</sup>*Friedrich Schiller University Jena, Abbe Center of Photonics, Albert-Einstein-Str. 6, 07745 Jena, Germany*

<sup>7</sup>*School of Physics, University of KwaZulu-Natal, Durban, South Africa*

<sup>8</sup>*National Institute of Theoretical Physics, UKZN Node, Durban, South Africa*

<sup>9</sup>*Department of Signal Theory and Communications,*

*Universitat Politècnica de Catalunya, Campus Nord D3, 08034 Barcelona, Spain*

<sup>10</sup>*National Metrology Institute of South Africa, Meiring Naudé Road, Brummeria, Pretoria 0040, South Africa*

Quantum teleportation allows protected information exchange between distant parties [1, 2], a crucial resource in future quantum networks [3]. Using high-dimensional quantum states for teleportation offers the promise of higher information capacity channels [4], protection against optimal cloning machines [5] and improved resilience to noise [6]. However, such promising advantages are limited by the commonly used linear optical detection schemes that require ancillary photons [7], where the number of entangled photons grows with the dimension of the quantum state to be teleported [8]. Here we overcome this restriction and experimentally realise the teleportation of high-dimensional states with just three photons, enabled by nonlinear optical detection. To create high-dimensional quantum states we employ photonic spatial modes and demonstrate a ten-dimensional teleportation channel, exceeding the state-of-the-art of two spatial modes for qubit teleportation [9–11] and qutrit teleportation with four [12] and five [13] photons. Our experimental scheme is not basis dependent and easily scaled in dimension without changing its three-photon configuration, making high-dimensional teleportation practically feasible for future high-bandwidth robust quantum networks.

Since its proposal in 1993 [1], quantum teleportation has played an important role in the progress of quantum information [14–16], and has acted as the stimulus for the development of many quantum concepts and technologies, notably measurement-based quantum computing [17], quantum gate [18] and trapped ion [19, 20] teleportation, quantum repeaters [21], long-distance quantum

communication [22, 23] and entanglement distribution [24, 25]. A large component of many of these schemes rely on the ability to teleport states that have high dimensions, but here experimental progress has been slow due to the significant experimental hurdle of the need to use ancillary photons in linear detection schemes, where  $d$  dimensions require approximately  $d$ -fold photon detection. Even state-of-the-art entanglement preparation and detection has achieved only 4 coincidences per hour for a 10-photon state [26], making high-dimensional teleportation practically infeasible. For this reason, while qubit quantum teleportation has been demonstrated with continuous [27–30] and discrete [31–33] variables, the state-of-the-art is still restricted to just three-dimensional states using path entanglement [12, 13]. Since the seminal work on orbital angular momentum (OAM) entanglement 20 years ago [34], spatial modes have become a popular avenue to access high-dimensional states [35–38], but here too only qubit teleportation has been demonstrated using OAM [9, 10] as well as in hybrid spin and OAM qubit states [11].

Several theoretical proposals have been made to extend teleportation from qubits to  $d$ -dimensional qudits using linear optics [39–41], but none have yet been realised experimentally for  $d > 3$ , with the present state-of-the-art ( $d = 3$ ) designed by a computer simulation [42] but still needing ancillary photons. Nonlinear optical approaches have been proposed [8, 43, 44], and used to perform a complete Bell state measurement, but only for qubit polarisation states [45], where ancillary photons are inconsequential. Inspired by these proposals, here we outline an experimental realisation, supported by a full theoretical treatment, of a nonlinear optical teleportation channel for arbitrary dimensions with just three photons, which we demonstrate using quantum states expressed as the spatial modes of light.

\*Electronic address: adam.valles@icfo.eu

†Electronic address: andrew.forbes@wits.ac.za

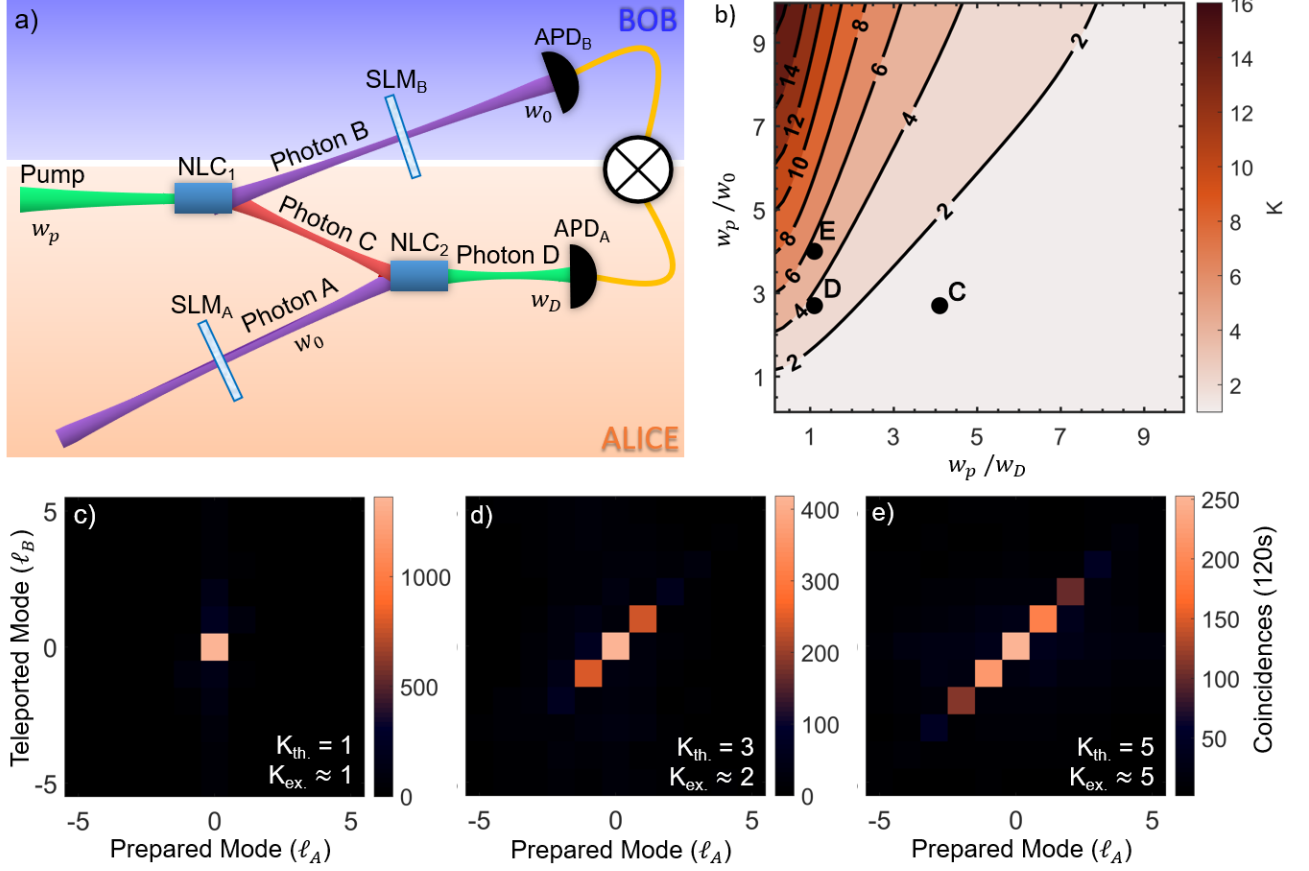


FIG. 1: **Realising a quantum teleportation channel based on nonlinear optical detection.** (a) A pump photon ( $\lambda_p = 532$  nm) undergoes spontaneous parametric downconversion (SPDC) in a nonlinear crystal (NLC<sub>1</sub>), producing a pair of entangled photons (signal B and idler C), at wavelengths of  $\lambda_B = 1565$  nm and  $\lambda_C = 808$  nm, respectively. Photon B is directed to a spatial mode detector comprising a spatial light modulator (SLM<sub>B</sub>) and a single mode fibre coupled avalanche photo-diode detector (APD). The state to be teleported is prepared as photon A using SLM<sub>A</sub> ( $\lambda_A = 1565$  nm), and is overlapped in a second nonlinear crystal (NLC<sub>2</sub>) with photon C, resulting in an upconverted photon D which is sent to a single mode fibre coupled APD. Photons B and D are measured in coincidence to find the joint probability of the prepared and measured states using the two SLMs. (b) The teleportation channel's theoretical modal bandwidth ( $K$ ) as a function of the pump ( $w_p$ ) and detected photons' ( $w_0$  and  $w_D$ ) radii, with experimental confirmation shown in (c) through (e) corresponding to parameter positions C, D and E in (b).  $K_{th.}$  and  $K_{ex.}$  are the theoretical and experimental teleportation channel capacities, respectively. and The cross-talk plots are shown as orbital angular momentum (OAM) modes prepared and teleported. The raw data is reported with no noise suppression or background subtraction.

## Results

**Experimental concept.** A schematic of our experiment is shown in Figure 1 (a) with full details provided in Supplementary Note 1. Two entangled photons, B and C, are produced from a nonlinear crystal (NLC<sub>1</sub>) configured for collinear non-degenerate spontaneous parametric downconversion (SPDC). Photon C is sent to interact with the state to be teleported (photon A), as prepared by Alice using a spatial light modulator (SLM<sub>A</sub>), while Bob measures the teleported photon B with a spatial light modulator (SLM<sub>B</sub>). In most teleportation schemes for qubits, the interaction of photons A and C takes the form of a Bell state analyser with linear optical elements (often combination of beam splitters and polarising beam

splitters), that renders the success of the teleportation a probabilistic process. However, beyond qubits, linear optical solutions result in mixed states [9] unless additional photons (ancillary photons) are added [8, 12, 13].

In our scheme we overlap photons A and C in a second nonlinear crystal (NLC<sub>2</sub>), and detect the frequency upconverted photon D, generated by means of sum frequency generation (SFG). The success of the teleportation process is conditioned on the measurement of the single photon D. We use a coherent state as input because the larger average number of photons in the coherent state enhances the probability for upconversion. All the photons in the coherent state carry the same modal information which we want to teleport. One such photon then takes part in the upconversion process to produce the photon that is detected to signal the teleportation of

the modal information to Bob's photon. One can consider the coherent input state and the output single photon state as *carriers* of the quantum information to be teleported, i.e., coherent superpositions of photonic spatial modes.

Noticeably, a linear optical Bell state analyser for qubits, that is a  $2 \times 2$  quantum gate, would ordinarily require two detectors, one for each of the photons A and C (often from the two output arms of the beam splitter); as more dimensions are added so too are photons, so that  $d$ -fold detection is needed. In the nonlinear version, there is only one upconverted photon, thus only one detector is needed regardless of dimension, eliminating the need for ancillary photons.

To better understand the teleportation process, it is instructive to use orbital angular momentum (OAM) modes as an example, with the full basis independent theoretical treatment given in the Supplementary Notes 2 through 4. We pump the SPDC crystal with a Laguerre Gaussian mode of azimuthal and radial indices  $\ell_p = 0$  and  $p_p = 0$ , respectively. OAM is conserved in the SPDC process [34] so that  $\ell_p = 0 = \ell_B + \ell_C$ . The upconversion process also conserves OAM [46], so if the detection is by a single mode fibre (SMF) that supports only spatial modes with  $\ell_D = 0$ , then  $\ell_D = 0 = \ell_A + \ell_C$ . One can see immediately that a coincidence is only detected when both A and B are the conjugate to C,  $\ell_A = \ell_B = -\ell_C$ , and thus the prepared state (A) matches the teleported state (B). One can show more generally (see Supplementary Note 2) that if the detection of photon D is configured to be into the same mode as the initial SPDC pump (we may call photon D the anti-pump), then the upconversion process acts as the conjugate of the SPDC process, and the state of photon A is teleported to photon B. However, upconversion aided teleportation only takes place under pertinent experimental conditions, namely, perfect anti-correlations between the signal and idler photons from the SPDC process in the chosen basis, and an upconversion crystal with length and phase-matching to ensure for anti-correlations between photons A and C (see Supplementary Note 3 for full details).

To find a bound on the modal capacity of the teleportation channel one can treat the teleportation process as a communication channel with an associated channel operator. This in turn can be treated as an entangled state, courtesy of the Choi-Jamioilowski state-channel duality [47], from which a Schmidt number ( $K$ ) can be calculated. We interpret this as the effective number of modes the channel can transfer (its modal capacity), given by

$$K = \frac{1}{\int T^2(\mathbf{k}_A, \mathbf{k}_B) d^2\mathbf{k}_A d^2\mathbf{k}_B}, \quad (1)$$

where

$$T(\mathbf{k}_A, \mathbf{k}_B) = \int \psi_{\text{SFG}}^*(\mathbf{k}_A, \mathbf{k}_C) \psi_{\text{SPDC}}(\mathbf{k}_C, \mathbf{k}_B) d\mathbf{k}_C,$$

with the SFG and SPDC mode functions expressed in the momentum ( $\mathbf{k}$ ) basis. Full details are given in Supple-

mentary Note 4. One finds that the controllable parameters are the beam radii of the pump ( $w_p$ ), and spatially filtered photons D ( $w_D$ ) and B ( $w_0$ ). Using Equation (1), we calculated the channel capacity for OAM modes, with the results shown in Figure 1 (b), revealing that a large pump mode relative to the detected teleported modes is optimal for capacity. A large pump mode with respect to the crystal length also increases the channel capacity, consistent with the well-known thin-crystal approximation. However, this comes at the expense of coincidence events, the probability of detecting the desired OAM mode, which must be balanced with the noise threshold in the system. We show three experimental examples of this trade-off in Figures 1 (c), (d) and (e), where the parameters for each can be deduced from the corresponding labelled positions in Figure 1 (b). The good agreement between the theoretical ( $K_{\text{th}}$ ) and experimentally measured ( $K_{\text{ex}}$ ) capacities validates the theory. Using the theory, we adjust the experimental parameters to optimise the teleportation channel, reaching a maximum of  $K \approx 10$  for OAM modes, as shown in the inset of Figure 2. This limit is not fundamental and is set only by our experimental resources. Nevertheless, we are able to establish a teleportation setup where the channel supports at least 10 OAM modes, exceeding the currently demonstrated limit of 3 modes with linear optics. The balance of channel capacity with noise is shown Figure 2. Using a probe of purity and dimension [48] we measure a decreasing fidelity with channel dimension, but always well above the upper bound of the fidelity achievable for classical teleportation, given by  $F_{\text{classical}} \leq \frac{2}{d+1}$  for  $d$  dimensions, shown as the classical limit (dashed line) in Figure 2 (full details in the Methods section).

**Teleportation results.** In Figure 3 (a) we show results for the teleportation channel in two, three and four dimensions. We confirm teleportation beyond just the computational basis by introducing a modal phase angle,  $\theta$ , on Bob's arm relative to Alice ( $\theta = 0$ ) for the two dimensional state  $|\Psi\rangle = |\ell\rangle + \exp(i\theta)|-\ell\rangle$  (we omit the normalisation throughout the text for simplicity). We vary the phase angle while measuring the resulting coincidences for three example OAM subspaces,  $\ell = \pm 1, \pm 2$  and  $\pm 3$ . The raw coincidences, without any noise subtraction, are plotted as a function of the phase angle in Figure 3 (a), confirming teleportation across all basis states. The resulting raw visibilities vary from 85% to 79%, with background subtracted visibilities all above 96% (see Supplementary Note 7 for full background subtraction results). Example results for the qutrit state  $|\Psi\rangle = |-1\rangle + |0\rangle + |1\rangle$  are shown in Figure 3 (b) as the real and imaginary parts of the density matrix, reconstructed by quantum state tomography, with the raw coincidences from the projections (in all orthogonal and mutually unbiased basis) shown in the inset. Without any noise subtraction the fidelity is  $F = 0.66$  ( $K = 5$  channel) and  $F = 0.78$  ( $K = 10$  channel), both well above the classical limit for a three-dimensional state. The values are

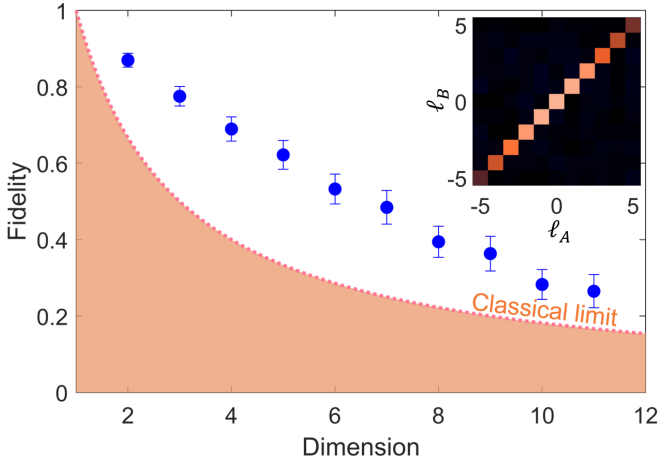


FIG. 2: **Quality of the teleportation process.** Experimental fidelities (points) for teleportation channel dimensions up to the maximum achievable channel capacity of  $K = 11 \pm 1$ , all well above the classical limit (dashed line). The inset shows the measured OAM modal spectrum of the optimised teleportation channel with maximum coincidences of 200 per second. The raw data is reported with no noise suppression or background subtraction.

consistent with the notion of noise increasing as the teleported state dimension approaches the channel capacity. With background subtraction the  $K = 5$  channel fidelity increases to  $F = 0.75$ , comparable to the lower noise  $K = 10$  channel.

Having replicated the present state-of-the-art, we proceed to illustrate the potential of the teleportation channel by sending four-dimensional states of the form  $|\Psi\rangle = |-3\rangle + \exp(i\theta_1)|-1\rangle + \exp(i\theta_2)|1\rangle + \exp(i\theta_3)|3\rangle$ , with inter-modal phases of  $\{\theta_1, \theta_2, \theta_3\} = \{-\pi/2, -\pi, -\pi/2\}, \{-\pi/2, 0, \pi/2\}, \{\pi/2, \pi, \pi/2\}$  and  $\{\pi/2, 0, -\pi/2\}$ . All possible outcomes from these mutually unbiased basis (MUBs) are shown in Figure 3 (c). We encoded each superposition (one at a time) in SLM<sub>A</sub> and projected photon B in each of the four states. The strong diagonal with little cross-talk confirms teleportation across all states. The inset shows an example state: the teleported state (solid bars) with the prepared state (transparent bars), for a similarity of  $S = 0.989$  (see description used in the Methods section).

The result in Figure 3 (c) also confirms that the channel is not basis dependent, since this superposition of OAM states is not itself an OAM eigenmode. To reinforce this message, we proceed to teleport  $d = 3$  and  $d = 9$  states in the Hermite-Gaussian (HG<sub>*n,m*</sub>) basis with indices  $n$  and  $m$ , with the results shown in Figure 4. In this basis the teleportation channel has a maximum capacity of  $K = 25$ . In both cases the teleported state (solid bars) is in very good agreement with the prepared state (transparent bars). A final summary of example teleported states is shown in Figure 5, covering dimensions two through nine, and across many bases. The prepared (transparent bars) and teleported (solid bars)

states are in good agreement, confirming the quality of the channel.

## Discussion and Conclusion

A Bell measurement based on SFG enables to implement a simple setup for teleportation, using the minimal number of two entangled photons. This teleportation protocol based on nonlinear detection had before only been experimentally realised for the teleportation of a photon's polarisation state [45]. Also there, a bright coherent state produced by a laser was used by the sender (A) in order to compensate the low upconversion efficiency of the nonlinear crystal (full details in the Supplementary Note 8). In both setups, an intrinsic characteristic of the state transfer process is that the sender does not need to know the quantum state to be teleported, a feature that differentiates quantum teleportation from remote state preparation [49]. In this sense, the input coherent state and the output single photon state can be considered as *carriers* of the protected information being teleported.

Remarkably, the rate of teleported photonic modal qubits here (one per second) is two orders of magnitude higher than that reported for polarisation qubits [45] (0.01 per second). The advance might be due to the quantum correlation between input and output spatial modes induced by the filtering for the  $\ell = 0$  upconverted photons. The teleportation efficiency could be increased quadratically by replacing the  $\ell = 0$  filter by a measurement of the OAM value of photon D. For result  $\ell = m$ , the teleportation operator reads  $\hat{T}_m = \sum_{\ell} |m - \ell\rangle_B \langle \ell|_C$  (with Schmidt coefficients omitted) and the resulting shift in OAM could be compensated by informing Bob to flip the received OAM value (e.g., with a dove prism) and to add  $m$  units of OAM to the output state.

Our results show teleportation of spatial states from  $d = 2$  to  $d = 9$  in a teleportation channel with tuneable dimensionality in any spatial basis, in the process setting a new state-of-the-art. Importantly, the approach brings high-dimensional teleportation within practical reach, eliminating a major experimental hurdle of curtailed efficiencies. Our results validate the non-classical nature of the channel without any noise suppression or background subtraction; with background subtraction we find excellent fidelities as reported in Supplementary Note 7. Importantly, our comprehensive theoretical treatment results in a simple expression that correctly predicts the modal capacity of the teleportation channel, which can be tuned by the modal sizes at the SPDC crystal and detectors, requiring only minor experimental adjustments (the focal length of the lenses, for example). The 10 dimensional channel for OAM modes and 25 dimensions for the HG modes highlights the exciting prospect this approach holds for teleportation of unknown high-dimensional spatial states, for example, images expressed in the pixel (position) basis. The modal capacity of our channel was

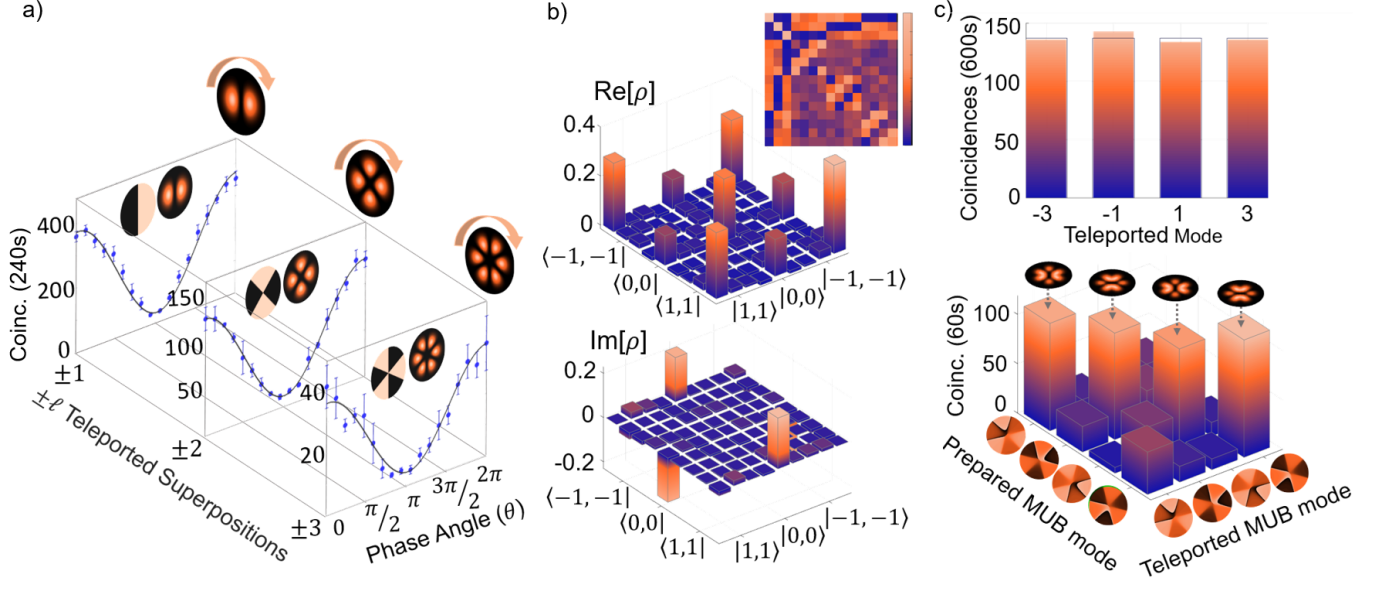


FIG. 3: **Visibilities and quantum state tomography.** (a) Measured coincidences (points) and fitted curve (solid) as a function of the phase angle ( $\theta$ ) of the corresponding detection analyser for the state  $|\phi\rangle = |\ell\rangle + \exp(i\theta)|-\ell\rangle$ , for three OAM subspaces of  $\ell = \pm 1, \pm 2$ , and  $\pm 3$  (further details in the Supplementary Note 5). (b) The real ( $\text{Re}[\rho]$ ) and imaginary ( $\text{Im}[\rho]$ ) parts of the density matrix ( $\rho$ ) for the qutrit state  $|\Psi\rangle = |-1\rangle + |0\rangle + |1\rangle$  as reconstructed by quantum state tomography. The inset shows the raw coincidences with maximum coincidences of 290 detected per second from the tomographic projections (full details in the Supplementary Note 6). (c) Measurements for teleportation of a 4-dimensional state, constructed from the states  $\ell = \{\pm 1, \pm 3\}$ , with the inset graph showing detection (solid bars) of all the prepared (transparent bars) OAM states comprising one of the MUB states. The raw data is reported with no noise suppression or background subtraction.

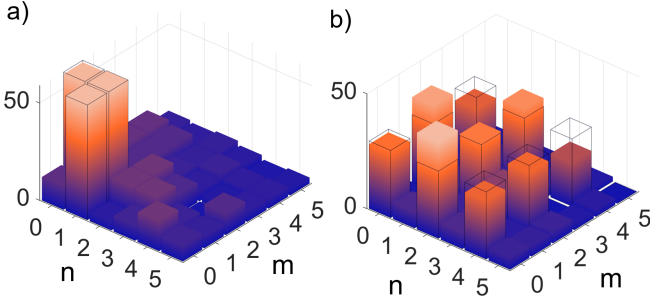


FIG. 4: **Teleportation in the Hermite-Gaussian basis.** Coincidence measurements for teleportation of a (a) 3-dimensional and (b) 9-dimensional  $\text{HG}_{n,m}$  state, constructed from the states  $(n, m) = \{(0, 1), (1, 0), (1, 1)\}$  and  $(n, m) = \{(0, 0), (2, 0), (0, 2), (2, 2), (2, 4), (4, 2), (4, 4)\}$ , respectively. The teleported state (solid bars) is in good agreement with the prepared state (transparent bars). The raw data is reported with no noise suppression or background subtraction.

limited only by experimental resources, while future research could target an increase of the number of teleported modes by optimising the choice of the relevant parameters, improved nonlinear processes, and flattening the Schmidt spectrum of the entangled two-photon state.

## Methods

### Fidelity

To quantify the quality of the teleportation process, we use the *fidelity*. It is defined for pure states as the squared magnitude of the overlap between the initial state that were to be teleported  $|\psi_A\rangle$  and the final teleported state that was received by Bob  $|\psi_B\rangle$ :

$$F = |\langle \psi_A | \psi_B \rangle|^2. \quad (2)$$

In the ideal case, where the teleported state is  $|\psi_B\rangle = \int \alpha(\mathbf{q}) \hat{a}_B^\dagger(\mathbf{q}) |\text{vac}\rangle d\mathbf{q}$  (full details in the Supplementary Note 1), the fidelity is  $F = 1$ . However, in a practical experiment, the conditions for the ideal case cannot be met exactly. Therefore, the fidelity is more generally given by

$$\begin{aligned} F &= \int \alpha^*(\mathbf{q}_B) \beta(\mathbf{q}_B) d^2 q_B \\ &= \int \alpha^*(\mathbf{q}_B) U^*(\mathbf{q}_D) g(\mathbf{q}_A, \mathbf{q}_D - \mathbf{q}_A, \mathbf{q}_D) \\ &\quad \times f(\mathbf{q}_B, \mathbf{q}_D - \mathbf{q}_A) \alpha(\mathbf{q}_A) d^2 q_B d^2 q_A d^2 q_D. \end{aligned} \quad (3)$$

It is possible to envisage a classical implementation of the state-transfer process. One would make a complete measurement of the initial state, send the information to Bob and he will then prepare the same state at his side. To ensure that the quantum teleportation process

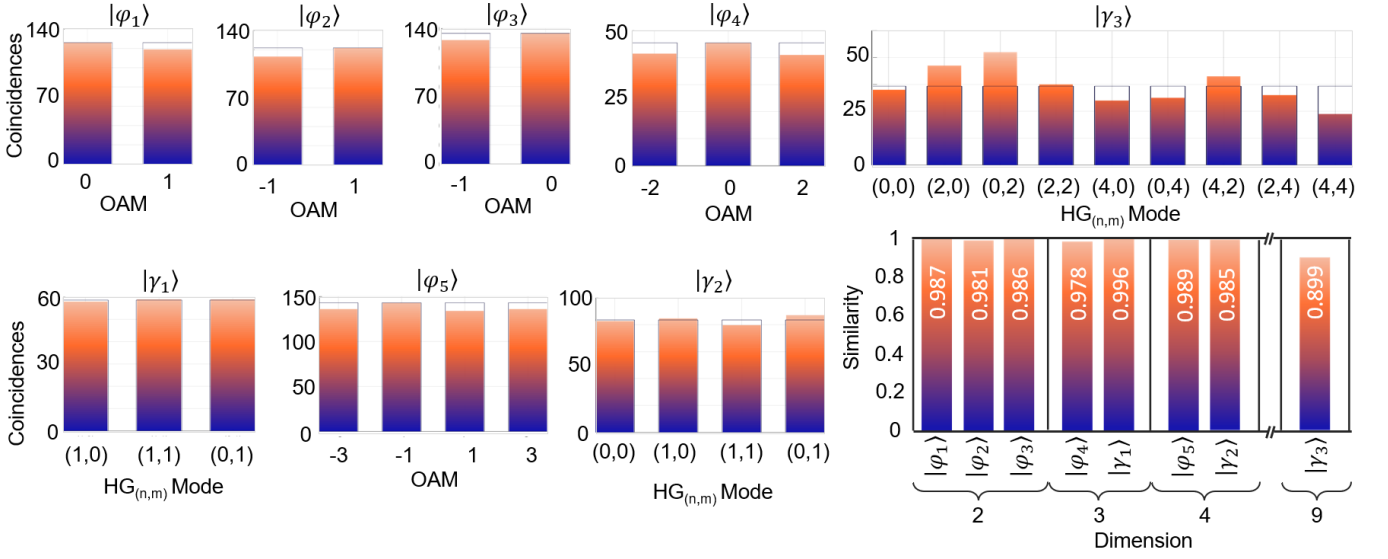


FIG. 5: **Summary of teleported states.** Similarities for teleportation of a 2,3,4 and 9-dimensional superposition states in the OAM (represented as  $|\varphi\rangle$ ) and HG (represented as  $|\gamma\rangle$ ) bases shown and labelled to the left. Teleported states are  $|\varphi_1\rangle = \frac{1}{\sqrt{2}}[|0\rangle + |-1\rangle]$ ,  $|\varphi_2\rangle = \frac{1}{\sqrt{2}}[|-1\rangle + |1\rangle]$ ,  $|\varphi_3\rangle = \frac{1}{\sqrt{2}}[|0\rangle - |1\rangle]$ ,  $|\varphi_4\rangle = \frac{1}{\sqrt{3}}[|-2\rangle + |0\rangle + |2\rangle]$ ,  $|\gamma_1\rangle = \frac{1}{\sqrt{3}}[|HG_{1,0}\rangle + |HG_{1,1}\rangle + |HG_{0,1}\rangle]$ ,  $|\varphi_5\rangle = \frac{1}{\sqrt{4}}[|-3\rangle - i|-1\rangle + |1\rangle + i|3\rangle]$ ,  $|\gamma_2\rangle = \frac{1}{\sqrt{4}}[|HG_{0,0}\rangle + |HG_{1,0}\rangle + |HG_{1,1}\rangle + |HG_{0,1}\rangle]$  and  $|\gamma_3\rangle = \frac{1}{\sqrt{9}}[|HG_{0,0}\rangle + |HG_{2,0}\rangle + |HG_{0,2}\rangle + |HG_{2,2}\rangle + |HG_{4,0}\rangle + |HG_{0,4}\rangle + |HG_{4,2}\rangle + |HG_{2,4}\rangle + |HG_{4,4}\rangle]$ . The raw data is reported with no noise suppression or background subtraction.

can outperform this classical state-transfer process, the fidelity of the process must be better than the maximum fidelity that the classical teleportation process can obtain.

In order to determine the classical bound on the fidelity by which we measure the teleported state  $|\psi\rangle$ , we define the probability to measure a value  $a$  by

$$P_\psi(a) = \langle \psi | \hat{E}_a | \psi \rangle, \quad (4)$$

where  $\hat{E}_a$  is an element of the positive operator valued measure (POVM) for the measurement of the initial state. These elements obey the condition

$$\sum_a \hat{E}_a = \mathbb{I}, \quad (5)$$

where  $\mathbb{I}$  is the identity operator. The estimated state associated with such a measurement result is represented by  $|\psi_a\rangle$ .

For the classical bound, we consider the average fidelity that would be obtained for all possible initial states. This average fidelity is given by

$$\begin{aligned} \mathcal{F} &= \int \sum_a P_\psi(a) |\langle \psi | \psi_a \rangle|^2 d\psi \\ &= \int \sum_a \langle \psi | \hat{E}_a | \psi \rangle |\langle \psi | \psi_a \rangle|^2 d\psi, \end{aligned} \quad (6)$$

where  $d\psi$  represents an integration measure over the Hilbert space of all possible input state. We assume that

this space is finite dimensional, but larger than just two-dimensional. Since all the states in this Hilbert space are normalized, the space is represented by a hyper-sphere. A convenient way to represent such an integral is with the aid of the Haar measure [50]. For this purpose, we represent an arbitrary state in the Hilbert space as a unitary transformation from some fixed state in the Hilbert space  $|\psi\rangle \rightarrow \hat{U}|\psi_0\rangle$ , so that  $d\psi \rightarrow dU$ . The average fidelity then becomes

$$\begin{aligned} \mathcal{F} &= \int \sum_a \langle \psi_a | \hat{U} | \psi_0 \rangle \langle \psi_0 | \hat{U}^\dagger \hat{E}_a \hat{U} | \psi_0 \rangle \langle \psi_0 | \hat{U}^\dagger | \psi_a \rangle dU \\ &= \int \sum_a \text{tr}\{\hat{\rho}_a \hat{U} \hat{\rho}_0 \hat{U}^\dagger \hat{E}_a \hat{U} \hat{\rho}_0 \hat{U}^\dagger\} dU, \end{aligned} \quad (7)$$

The general expression for the integral of the tensor product of four such unitary transformations, represented as matrices, is given by

$$\begin{aligned} &\int U_{ij}(U^\dagger)_{kl} U_{mn}(U^\dagger)_{pq} dU \\ &= \frac{1}{d^2 - 1} (\delta_{il} \delta_{jk} \delta_{mq} \delta_{np} + \delta_{iq} \delta_{jp} \delta_{ml} \delta_{nk}) \\ &\quad - \frac{1}{(d^2 - 1)d} (\delta_{il} \delta_{jp} \delta_{mq} \delta_{nk} + \delta_{iq} \delta_{jk} \delta_{ml} \delta_{np}). \end{aligned} \quad (8)$$

Using this result in Eq. (7), we obtain

$$\mathcal{F} = \frac{1}{(d+1)d} \left( d + \sum_a \langle \psi_a | \hat{E}_a | \psi_a \rangle \right), \quad (9)$$



where  $d$  is the dimension of the Hilbert space and where we imposed  $\text{tr}\{\hat{\rho}_0\} = \text{tr}\{\hat{\rho}_0^2\} = \text{tr}\{\hat{\rho}_a\} = 1$ . We see that  $\mathcal{F}$  is maximal if  $E_a$  represents rank 1 projectors and  $E_a|\psi_a\rangle = |\psi_a\rangle$ , i.e.  $E_a = |\psi_a\rangle\langle\psi_a|$ . Then  $\sum_a \langle\psi_a|\hat{E}_a|\psi_a\rangle = d$ . It follows that the upper bound of the fidelity achievable for the classical state-transfer process is given by

$$\mathcal{F} \leq \frac{2}{d+1}. \quad (10)$$

The fidelity obtained in quantum teleportation needs to be better than this bound to outperform classical scheme.

### Similarity

We use a normalised distance measure to quantify the quality of the state being teleported, denoted the *Similarity* (S),

$$S = 1 - \frac{\sum_j |(|C_j^{Ex.}|^2 - |C_j^{Th.}|^2)|}{\sum_j |C_j^{Ex.}|^2 + \sum_j |C_j^{Th.}|^2}. \quad (11)$$

Here we take the normalised intensity coefficients,  $|C_j^{Th.}|^2$ , encoded onto SLM<sub>A</sub> for the  $j$ th basis mode comprising the state being teleported (i.e.  $|\Phi\rangle = \sum_j C_j |j\rangle$ ) and compare it with the corresponding  $j$ th coefficient  $|C_j^{Ex.}|^2$  detected after traversing the teleportation channel (made with  $j$ th-mode projections on SLM<sub>B</sub>) as described in the Supplementary Note 4. A small difference in values between encoded and detected state would result in a small 'distance' between the prepared and received value. As such, the second term in Eq. (11) diminishes with increasing likeness of the states, causing the Similarity measure to tend to 1 for unperturbed teleportation of the state.

### Dimensionality measurements

We measured the dimensions of our teleportation channel by probing it with multiple superposition states,  $|M, \theta\rangle_n$ , for  $M = n/2$ , with each state indexed by  $n$ . In the OAM basis, i.e.  $|\ell\rangle \in \mathcal{H}_d$ , we construct the projection holograms from the states

$$U_n(\phi, \theta) = \mathcal{M} \sum_{k=0}^{n-1} \exp(i\Phi_M(\phi; \beta_k \oplus \theta)), \quad (12)$$

constructed from superpositions of fractional OAM modes,

$$\exp(i\Phi_M(\phi; \alpha)) = \begin{cases} e^{iM(2\pi+\phi-\alpha)} & 0 \leq \phi < \alpha \\ e^{iM(\phi-\alpha)} & \alpha \leq \phi < 2\pi \end{cases}, \quad (13)$$

having the same charge,  $M = n/2$ , but rotated by an angle  $\beta_k \oplus \alpha = \text{mod}\{\beta_k + \alpha, 2\pi\}$  for  $\beta_k = \frac{2\pi}{n}k$ .

In the OAM basis  $\theta$  corresponds to the relative rotation of the holograms. After transmitting the photon imprinted with the state  $|M, \theta\rangle_n$ , through the teleportation channel,  $\hat{T} = \sum_\ell \lambda_\ell |\ell\rangle_A \langle\ell|_B$ , the teleported photon is projected onto the state  $|M, 0\rangle_n$ . The detection probability is then given by

$$P_n(\theta) = |\langle 0, M | \hat{T} | M, \theta \rangle|^2, \quad (14)$$

having a peak value at  $P(\theta = 0)$  and a minimum at  $P(\theta = \pi/n)$ . In the experiment, there are noise contributions which can be attributed to noise from the environment, dark counts and from the downconversion and upconversion processes. Since the channel is isomorphic to an entangled state, i.e

$$\hat{T} = \sum_\ell \lambda_\ell |\ell\rangle_A \langle\ell|_B \rightarrow \rho_{\hat{T}} := \sum_\ell \lambda_\ell |\ell\rangle_A \langle\ell|_B, \quad (15)$$

we represent the system by an isotropic state,

$$\rho = p\rho_{\hat{T}} + (1-p)\mathbb{I}_d^2/d^2, \quad (16)$$

where  $p$  is the probability of teleporting a state through the channel or equivalently the purity and  $\mathbb{I}_d^2$  is a  $d^2$  dimensional identity matrix. In this case, the detection probability is given by

$$P_n(\theta) = |\langle 0, M | \hat{T} | M, \theta \rangle|^2 + (1-p)/d^2 I_n(\theta), \quad (17)$$

where  $I_n(\theta) = |\langle 0, M | \mathbb{I}_{d^2} | M, \theta \rangle|^2$ .

We compute the visibilities

$$V_n = \frac{|P_n(0) - P_n(\pi/n)|}{|P_n(0) + P_n(\pi/n)|}. \quad (18)$$

Using the fact that the visibility,  $V_n := V_n(p, d)$ , obtained for each analyser indexed by,  $n = 1, 3, \dots, 2N-1$ , scales monotonically with  $d$  and  $p$  [48], we determine the optimal  $(p, d)$  pair that best fit the function  $V_n(p, K)$  to all  $N$  measured visibilities by employing the method of least squares (LSF).

Furthermore, the teleportation fidelity for each subspace within the  $d$  dimensional state,  $\rho$ , can be computed by truncating the density matrix and overlapping it with a state that has perfect correlations, i.e. using a maximally entangled state as a dual state of channel.

### Acknowledgements

B.S. would like to acknowledge the Department of Science and Innovation and Council for Industrial and Scientific Research (South Africa) for funding. A.V. acknowledges the Japan Society for the Promotion of Science for funding (JSPS-KAKENHI - G21K14549). F.S. acknowledges financial support by the Fraunhofer Internal Programs under Grant No. Attract 066-604178. M.A.C. and A.F. thanks the National Research Foundation for funding. A.V. and J.T. acknowledge financial support from the "Severo Ochoa" program

for Centres of Excellence CEX2019-000910-S [MICINN/AEI/10.13039/501100011033], Fundació Cellex, Fundació Mir-Puig, and Generalitat de Catalunya through CERCA, from project 20FUN02 “POLight” funded by the EMPIR programme, and from project QUISPAMOL (PID2020-112670GB-I00).

#### **Author contributions**

The experiment was performed by B.S., A.V. and I.N., with technical support by M.C., and the theory developed by F.S., T.K., J.T., and F.R. Data analysis was performed by B.S., A.V., I.N. and A.F. and the experiment was conceived by A.V., F.S., T.K., J.T., F.R. and A.F. All authors contributed to the writing of the manuscript. A.F. supervised the project.

#### **Competing Interests**

The authors declare no competing interests.

#### **Data availability**

The data that supports the plots within this paper and other findings of this study are available from the corresponding author upon reasonable request.



# Supplementary Information: High-dimensional spatial teleportation enabled by nonlinear optics

## I. EXPERIMENTAL SETUP

We refer the reader to the detailed schematic of our experiment found in Fig. S6. Here a 1.5 W linearly polarised continuous wave (CW) Coherent Verdi laser centred at a wavelength of  $\lambda = 532$  nm was focused down using a  $f_1 = 750$  mm lens to produce a spot size of  $w_p \approx 600 \mu\text{m}$  in a periodically-poled potassium titanyl phosphate (PPKTP) crystal ( $\text{NLC}_1$ ), yielding signal and idler photons at wavelengths  $\lambda = 1565$  nm and 808 nm. A HWP placed before the crystal facilitated polarisation matching. A 750 nm longpass filter (LPF) placed directly after the crystal blocked the unconverted pump beam, while a long-pass dichroic mirror ( $\text{DM}_1$ ) centred at  $\lambda = 950$  nm transmitted the  $\lambda = 1565$  nm down-converted photon through to the receiver party (labelled 'Bob') and reflected the 808 nm down-converted photons. The reflected photon was imaged with a 1:1 imaging 4f system (focal lengths of  $f_2, f_3 = 175$  mm) onto a second PPKTP crystal ( $\text{NLC}_2$ ) for sum-frequency generation (SFG).

Both crystals used for up- and down-conversion were  $1 \times 2 \times 5$  mm periodically-poled potassium titanyl phosphate (PPKTP) crystal with poling period  $9.675 \mu\text{m}$  for type-0 phase matching. They were spatially orientated so that frequency conversion occurred for vertically polarised pump (and seed) light, producing vertically polarised photons. Phase matching for collinear generation of 1565 nm and 808 nm SPDC as well as upconversion of 808 nm photons with the 1565 nm structured pump was achieved through control of the crystal temperatures. Here the optimal temperatures were found to be  $27.3^\circ\text{C}$  and  $65^\circ\text{C}$  respectively.

The intense state to be teleported was created by a phase-only modulation by a spatial light modulator ( $\text{SLM}_A$ ) of a 2W horizontally polarised EDFA amplified 1565 nm laser that was expanded onto  $\text{SLM}_A$  with a telescope of  $f_4 = 50$  mm and  $f_5 = 150$  mm. The polarisation of the modulated light was rotated to vertical using a second HWP to meet the phase-matching condition for SFG. A second 4f 10:1 imaging telescope (focal lengths  $f_6 = 750$  mm and  $f_7 = 75$  mm, respectively) with an aperture (A) in the Fourier plane resized and isolated the 1st diffraction order of the modulated beam from the SLM. The prepared state then formed a  $200 \mu\text{m}$  spot size in the second PPKTP crystal and was overlapped with the 808 nm photons by means of another long-pass dichroic mirror centered at 950 nm ( $\text{DM}_2$ ) to generate up-converted photons of 532 nm. A  $532 \pm 3$  nm band-pass filter ( $\text{BPF}_{532}$ ) after the crystal blocked the residual down-converted photons and 1565 nm modulated pump beam, allowing the up-converted photons to be imaged onto a single-mode fiber (SMF) with a  $f_8 = 750$  mm and

$f_9 = 4.51$  mm 4f telescope. The photons were detected with a Perkin-Elmer VIS avalanche photodiode (APD) and in coincidence with the photon sent to 'Bob'.

The transmitted  $\lambda = 1565$  nm down-converted photons sent to 'Bob' were expanded and imaged onto a second SLM with two 4f imaging systems (focal lengths of  $f_{10} = 100$  mm,  $f_{11} = 200$  mm,  $f_{12} = 150$  mm and  $f_{13} = 750$  mm) for spatial tomographic projections of the teleported state. Here the spatially modulated photons were then filtered with an aperture and resized (4f telescope with focal lengths  $f_{14} = 750$  mm and  $f_{15} = 2.0$  mm) for coupling into an SMF at  $\lambda = 1565$  nm, which was detected by an IDQuantique ID220 InGaS free-running APD. A PicoQuant Hydraharp 400 event timer allowed the projected SFG and SPDC photons to be measured in coincidence (C.C.) on the pico-second time scale.

## II. TELEPORTATION WITH SUM-FREQUENCY GENERATION

The general scheme for quantum teleportation is used here, developed as in Refs. [8, 51]. However, the state that is teleported is a multi-dimensional single-photon state — i.e., the spatial mode is selected from a multi-dimensional set. The quantum state to be teleported can be represented by

$$|\psi_A\rangle = \int \alpha(\mathbf{q}_A) \hat{a}_A^\dagger(\mathbf{q}_A) |\text{vac}\rangle d^2 q_A, \quad (19)$$

where  $\alpha(\mathbf{q}_A)$  is the angular spectrum associated with the chosen spatial mode,  $\hat{a}_A^\dagger(\mathbf{q}_A)$  is the creation operator of photons with two-dimensional transverse wave vector  $\mathbf{q}_A$  and  $|\text{vac}\rangle$  is the vacuum state. It is assumed that the frequency  $\omega_A$  is fixed.

Using SPDC, we prepare an entangled state and consider a single pair of photons with transverse wave vectors  $\mathbf{q}_B$  and  $\mathbf{q}_C$ , respectively. The state of this photon pairs can be expressed by

$$|\psi_{BC}\rangle = \int f(\mathbf{q}_B, \mathbf{q}_C) \hat{a}_B^\dagger(\mathbf{q}_B) \times \hat{a}_C^\dagger(\mathbf{q}_C) |\text{vac}\rangle d^2 q_B d^2 q_C, \quad (20)$$

where  $f(\mathbf{q}_B, \mathbf{q}_C)$  is the two-photon wave function. The state of the combined system is then given by

$$\begin{aligned} |\psi_{ABC}\rangle &= |\psi_A\rangle \otimes |\psi_{BC}\rangle \\ &= \int \alpha(\mathbf{q}_A) f(\mathbf{q}_B, \mathbf{q}_C) \hat{a}_A^\dagger(\mathbf{q}_A) \hat{a}_B^\dagger(\mathbf{q}_B) \\ &\quad \times \hat{a}_C^\dagger(\mathbf{q}_C) |\text{vac}\rangle d^2 q_A d^2 q_B d^2 q_C, \end{aligned} \quad (21)$$

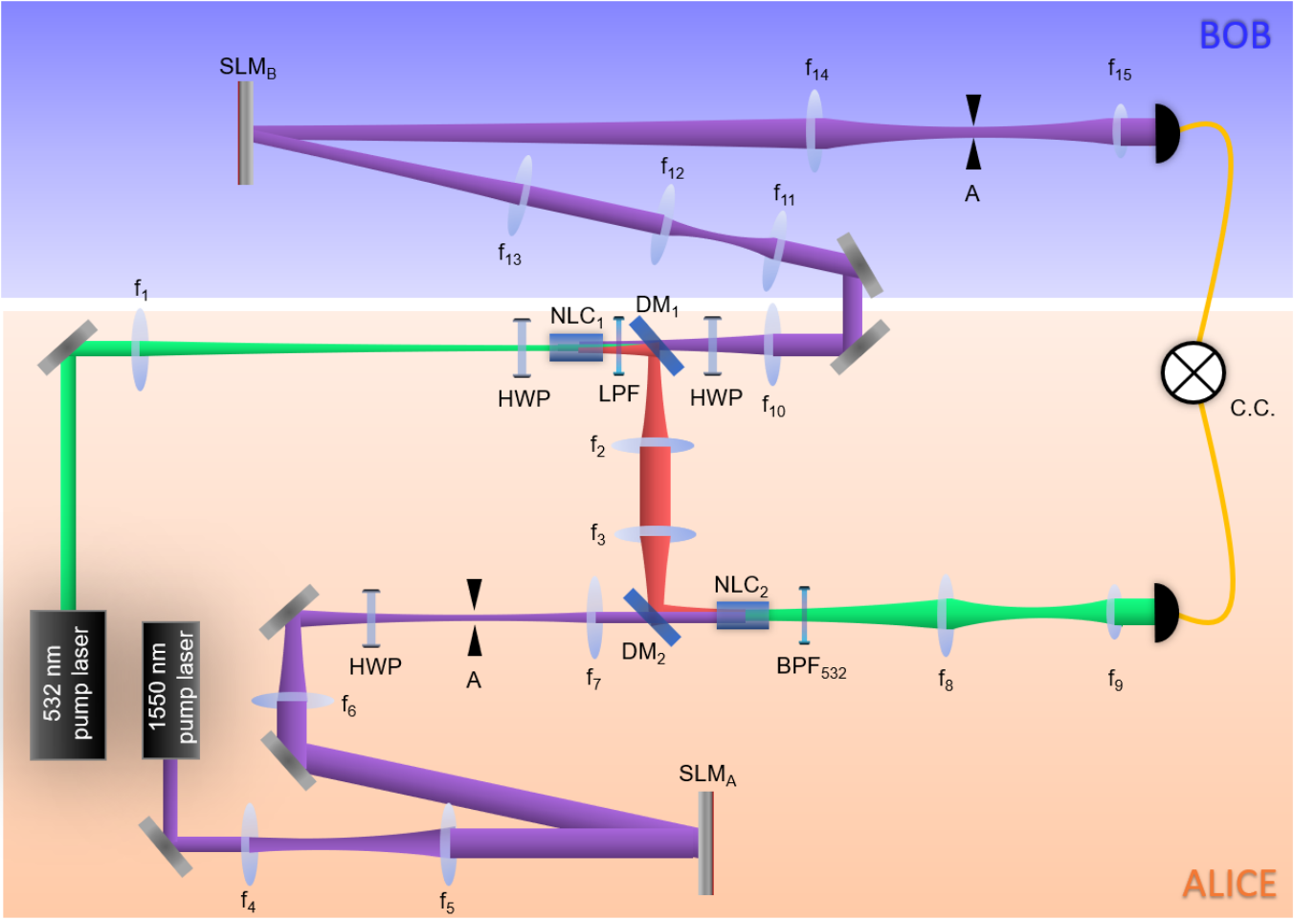


FIG. 6: Detailed experimental setup description for high-dimensional spatial teleportation without ancillary photons.

The process of sum-frequency generation (SFG) is now applied to the state in Eq. (21) to produce an unconverted photon  $D$  from the pair of photons  $A$  and  $C$ . The resulting quantum state of the system becomes

$$|\psi_{BD}\rangle = \int g(\mathbf{q}_A, \mathbf{q}_C, \mathbf{q}_D) f(\mathbf{q}_B, \mathbf{q}_C) \alpha(\mathbf{q}_A) \hat{a}_B^\dagger(\mathbf{q}_B) \times \hat{a}_D^\dagger(\mathbf{q}_D) |\text{vac}\rangle d^2q_A d^2q_B d^2q_C d^2q_D, \quad (22)$$

where  $g(\mathbf{q}_A, \mathbf{q}_C, \mathbf{q}_D)$  is the kernel for the SFG process.

If we assume the critical phase-matching condition  $\mathbf{q}_A + \mathbf{q}_C = \mathbf{q}_D$ , then the expression becomes

$$|\psi_{BD}\rangle = \int g(\mathbf{q}_A, \mathbf{q}_D - \mathbf{q}_A, \mathbf{q}_D) f(\mathbf{q}_B, \mathbf{q}_D - \mathbf{q}_A) \alpha(\mathbf{q}_A) \times \hat{a}_B^\dagger(\mathbf{q}_B) \hat{a}_D^\dagger(\mathbf{q}_D) |\text{vac}\rangle d^2q_A d^2q_B d^2q_D, \quad (23)$$

where we eliminate  $\mathbf{q}_C$  in terms of  $\mathbf{q}_A$  and  $\mathbf{q}_D$ . From the arguments of  $f$ , we see that the wave vector of photon  $A$  is now related to that of the teleportation photon  $B$ .

With the aid of a projective measurement of the SFG photon  $D$  in terms of a mode  $U(\mathbf{q}_D)$ , analogous to projecting into one of the Bell states, we can herald the teleportation of the state. The state of Bob's photon  $B$  is

then given by

$$|\psi_B\rangle = \int \beta(\mathbf{q}_B) \hat{a}_B^\dagger(\mathbf{q}_B) |\text{vac}\rangle d^2q_B, \quad (24)$$

where

$$\beta(\mathbf{q}_B) = \int U^*(\mathbf{q}_D) g(\mathbf{q}_A, \mathbf{q}_C, \mathbf{q}_D) \times f(\mathbf{q}_B, \mathbf{q}_C) \alpha(\mathbf{q}_A) d^2q_A d^2q_C d^2q_D. \quad (25)$$

A successful teleportation process would imply that  $\beta(\mathbf{q}) = \alpha(\mathbf{q})$ . It requires that

$$\int U^*(\mathbf{q}_D) g(\mathbf{q}_A, \mathbf{q}_C, \mathbf{q}_D) \times f(\mathbf{q}_B, \mathbf{q}_C) d^2q_C d^2q_D \approx \delta(\mathbf{q}_B - \mathbf{q}_A). \quad (26)$$

Under what circumstance would this condition be satisfied? First, we'll assume that the mode  $U(\mathbf{q})$  for the measurement of the SFG photon  $D$  (the so-called *anti-pump*) is the same as the mode of the pump beam. The SFG process can then be regarded as the conjugate of the

SPDC process, used to produce the entangled photons. Hence,

$$\int U^*(\mathbf{q}_D)g(\mathbf{q}_A, \mathbf{q}_C, \mathbf{q}_D) d^2q_D \sim f^*(\mathbf{q}_A, \mathbf{q}_C). \quad (27)$$

The two-photon wave function is a product of the pump mode and the phase-matching function, which is in the form of a sinc-function:

$$f(\mathbf{q}_B, \mathbf{q}_C) \sim U(\mathbf{q}_B + \mathbf{q}_C) \text{sinc}(\eta|\mathbf{q}_B - \mathbf{q}_C|^2), \quad (28)$$

where  $\eta$  represents a dimension parameter that determines the width of the function (see below). Under suitable experimental conditions (discussed below) the sinc-function only contributes when its argument is close to zero so that the sinc-function can be replaced by 1. Moreover, if the modes for the pump and the anti-pump are wide enough, they can be regarded as plane waves, which are represented as Dirac  $\delta$  functions in the Fourier domain. Then

$$f(\mathbf{q}_B, \mathbf{q}_C) \approx \delta(\mathbf{q}_B + \mathbf{q}_C), \quad (29)$$

and

$$\int U^*(\mathbf{q}_D)g(\mathbf{q}_A, \mathbf{q}_C, \mathbf{q}_D) d^2q_D \approx \delta(\mathbf{q}_A + \mathbf{q}_C). \quad (30)$$

Together, they produce the required result in Eq. (26) after the integration over  $\mathbf{q}_C$  has been evaluated.

It follows that, by detecting the up-converted photon  $D$ , the state of photon  $B$  held by Bob is heralded to be

$$|\psi_B\rangle = \int \alpha(\mathbf{q}) \hat{a}_B^\dagger(\mathbf{q}) |\text{vac}\rangle d\mathbf{q}. \quad (31)$$

It means that the teleportation process can be performed successfully with SFG, provided that the applied approximation are valid under the pertinent experimental conditions, which are considered next.

### III. EXPERIMENTAL CONDITIONS

It is well-known that SPDC produces pairs of photons (signal and idler) that are entangled in several degrees of freedom, including energy-time, position-momentum and spatial modes. A good review covering these scenarios is found in Ref. [52]. With SPDC being a suitable source of entanglement for our protocol, we consider in more detail what the experimental conditions need to be to achieve successful teleportation with the aid of SFG. For this purpose, we consider a collinear SPDC system with some simplifying assumptions. Even though details may be different from a more exact solution, the physics is expected to be the same.

As shown in the previous section, the success of the process requires that  $\mathbf{q}_B = -\mathbf{q}_C$ , which implies perfect anti-correlation of the wave vectors between the signal

(photon  $B$ ) and idler (photon  $C$ ). It is achieved when (a) the argument of the sinc-function can be set to zero, which is valid under the *thin-crystal approximation*, and (b) the beam waist of the pump beam  $w_p$  is relatively large, leading to the *plane-wave approximation*.

The scale of the sinc-function is inversely proportional to  $\sqrt{\lambda_p L}$  where  $\lambda_p$  is the wavelength of pump (or anti-pump) and  $L$  is the length of the nonlinear crystal ( $L = 5$  mm in our case). To enforce the requirement that its argument is evaluate close to zero, we require that the integral only contains significant contributions in this region. Therefore, the angular spectrum of the pump mode with which it is multiplied, must be much narrower than the sinc-function. The width of the angular spectrum of the pump mode is inversely proportional to the beam width  $w_p$ . Therefore, the condition requires that

$$\frac{1}{\lambda_p L} \gg \frac{1}{w_p^2} \Rightarrow 1 \gg \frac{\lambda_p L}{w_p^2} \propto \frac{L}{z_R}, \quad (32)$$

where  $z_R$  is the Rayleigh range of the pump beam. The relationship shows that the sinc-function can be replaced by 1 if the Rayleigh range of the pump beam is much larger than the length of the nonlinear crystal, leading to the thin-crystal approximation. We see that this condition is consistent with the requirement that  $w_p$  is relatively large, which is required for the plane-wave approximation.

Similar conditions are required for the second nonlinear crystal that performs sum-frequency generation. In that case, two input photons with angular frequencies  $\omega_A$  and  $\omega_C$ , respectively, are annihilated to generate a photon with an angular frequency  $\omega_D = \omega_A + \omega_C$ , imposed by energy conservation. The size of the mode that is detected, takes on the role of  $w_p$  and the length of the second nonlinear crystal replaces the length  $L$  of the first crystal. The wavelength after the sum-frequency generation process is the same as that of the pump for the SPDC  $\lambda_p$ . The equivalent conditions impose an anti-correlation  $\mathbf{q}_A = -\mathbf{q}_C$ , as implied in Eq. (30).

### IV. TELEPORTATION CHANNEL

In order to simulate the teleportation process, one may view it as a communication channel with imperfections such as loss and a limited bandwidth. The operation that represents the teleportation channel may be obtained by overlapping a photon from the SPDC state with one of the inputs for the SFG process, where the SPDC state is  $|\psi_{\text{SPDC}}\rangle = |\psi_{B,C}^{(\text{SPDC})}\rangle$ , as defined in Eq. (20). The two-photon wave function, which is symbolically provided in Eq. (28) can be represented more accurately as

$$f_{\text{SPDC}}(\mathbf{q}_B, \mathbf{q}_C) = \mathcal{N} \exp(-\frac{1}{4}w_p^2|\mathbf{q}_B + \mathbf{q}_C|^2) \times \text{sinc}(\frac{1}{2}L_p \Delta k_z), \quad (33)$$

where  $\mathcal{N}$  is a normalisation constant,  $w_p$  is the pump beam radius, and  $L_p$  is the nonlinear crystal length. The

mismatch in the z-components of the wave vectors for non-degenerate collinear quasi-phase matching is

$$\Delta k_z = -\frac{\lambda_p}{4\pi n_p}|\mathbf{q}_B + \mathbf{q}_C|^2 + \frac{\lambda_B}{4\pi n_B}|\mathbf{q}_B|^2 + \frac{\lambda_C}{4\pi n_C}|\mathbf{q}_C|^2, \quad (34)$$

where,  $\lambda_{B,C}$  are the down-converted wavelengths in vacuum for the signal and idler, respectively, with their associated crystal refractive indices  $n_B$  and  $n_C$ , and  $\lambda_p$  is the pump wavelength in vacuum, with its associated crystal refractive index denoted by  $n_p$ . The quasi-phase matching condition is implemented by periodic poling of the nonlinear medium. It implies a slight reduction in efficiency by a factor  $2/\pi$ , which is absorbed into the normalisation constant.

The SFG process may be thought of as the SPDC case in reverse where photons  $C$  and  $A$  (with wave vectors  $\mathbf{q}_C$  and  $\mathbf{q}_A$ , respectively) are upconverted to an 'anti-pump' photon  $D$ . It can thus be represented, in analogy to Eq. (28), by the bra-vector

$$\langle \psi_{C,A}^{(\text{SFG})} | = \int \langle \text{vac} | \hat{a}_C(\mathbf{q}_C) \hat{a}_A(\mathbf{q}_A) \times f^*(\mathbf{q}_C, \mathbf{q}_A) d^2 q_C d^2 q_A, \quad (35)$$

where the associated two-photon wave function is given by

$$f_{\text{SFG}}^*(\mathbf{q}_C, \mathbf{q}_A) = \mathcal{N} \exp(-\frac{1}{4}w_D^2|\mathbf{q}_C + \mathbf{q}_A|^2) \times \text{sinc}(\frac{1}{2}L_D\Delta k_z), \quad (36)$$

with  $w_D$  being the anti-pump beam radius (replacing  $w_p$ ), and  $L_D$  being the nonlinear crystal length (replacing  $L_p$ ). The wave vector mismatch  $\Delta k_z$  differs from the expression in Eq. (34) only in the replacement of  $\mathbf{q}_B$  by  $\mathbf{q}_A$  and a possible different value for  $\Lambda$ .

We can now define a *teleportation channel operator* as the partial overlap between  $|\psi_{B,C}^{(\text{SPDC})}\rangle$  and  $\langle \psi_{C,A}^{(\text{SFG})} |$ , where only the photons associated with  $C$  are contracted. The resulting operator is given by

$$\hat{T} = \langle \psi_{C,A}^{(\text{SFG})} | \psi_{B,C}^{(\text{SPDC})} \rangle = \int |\mathbf{q}_B\rangle T(\mathbf{q}_B, \mathbf{q}_A) \langle \mathbf{q}_A | d^2 q_A d^2 q_B, \quad (37)$$

where  $|\mathbf{q}_B\rangle = \hat{a}_B^\dagger(\mathbf{q}_B)|\text{vac}\rangle$ , and  $\langle \mathbf{q}_A | = \langle \text{vac} | \hat{a}_A(\mathbf{q}_A)$ . The kernel for the channel is given by

$$T(\mathbf{q}_B, \mathbf{q}_A) = \int f_{\text{SFG}}^*(\mathbf{q}_C, \mathbf{q}_A) f_{\text{SPDC}}(\mathbf{q}_B, \mathbf{q}_C) d^2 q_C. \quad (38)$$

It describes how spatial information is transferred by the teleportation process, implemented with SFG.

The teleportation process can be simplified by using the thin-crystal approximation, discussed above. The Rayleigh ranges of the pump beam and anti-pump

beam are made much larger than their respective crystal lengths. Therefore,  $L/z_R \rightarrow 0$ , for both the pump and the anti-pump. It allows us to approximate the phase-matching sinc-functions in Eqs. 33 and 36 as Gaussian functions [53]

$$\text{sinc}(\frac{1}{2}L\Delta k_z) \rightarrow \exp(-L\Delta k_z). \quad (39)$$

where  $\kappa$  is a numerical constant. The wave functions then become

$$f_{\text{SPDC}}(\mathbf{q}_B, \mathbf{q}_C) = \mathcal{N} \exp(-\frac{1}{4}w_p^2|\mathbf{q}_B + \mathbf{q}_C|^2) \times \exp[-L_p\Delta k_z(\mathbf{q}_B, \mathbf{q}_C)], \quad (40)$$

and

$$f_{\text{SFG}}^*(\mathbf{q}_C, \mathbf{q}_A) = \mathcal{N} \exp(-\frac{1}{4}w_D^2|\mathbf{q}_C + \mathbf{q}_A|^2) \times \exp[-L_D\Delta k_z(\mathbf{q}_C, \mathbf{q}_A)], \quad (41)$$

where  $\Delta k_z$  is given by Eq. (34).

Substituting Eq. 40 and 41 into Eq. 38, we obtain

$$T(\mathbf{q}_B, \mathbf{q}_A) = \mathcal{N}^2 \int \exp[-\frac{1}{4}w_p^2|\mathbf{q}_B + \mathbf{q}_C|^2 - \frac{1}{4}w_D^2|\mathbf{q}_C + \mathbf{q}_A|^2 - L_p\Delta k_z(\mathbf{q}_B, \mathbf{q}_C) - L_D\Delta k_z(\mathbf{q}_C, \mathbf{q}_A)] d^2 q_C. \quad (42)$$

If we set  $L_p = L_D = 0$  and evaluate the integral, we obtain the thin-crystal limit expression

$$T(\mathbf{q}_B, \mathbf{q}_A) = \frac{\mathcal{N}^2}{\pi(w_D^2 + w_p^2)} \times \exp\left[-\frac{w_D^2 w_p^2}{4(w_D^2 + w_p^2)}|\mathbf{q}_B - \mathbf{q}_A|^2\right] = T'(\mathbf{q}_B - \mathbf{q}_A). \quad (43)$$

According to the Choi-Jamolkowski (state-channel) duality, we can treat the channel operation in Eq. (42) as an entangled state. It can thus be used to calculate a Schmidt number for the state, which can be interpreted as the effective number of modes that the channel can transfer. For this purpose, we set  $L_p = L_D = L$ . The result is

$$\kappa = \frac{n_A n_B w_D^2 w_p^2}{(w_D^2 + w_p^2)(n_A \lambda_B + n_B \lambda_A)L}, \quad (44)$$

up to some numerical factor of order 1. Although the Schmidt number provides an indication of the number of modes that can be transferred by the teleportation process, it does not tell us what the modes are that can be transferred. For this purpose, we investigate the system numerically.

## V. NUMERICAL SIMULATION

It follows that Eq. (43) can be used to simulate the conditional probabilities for encoding and detecting spatial

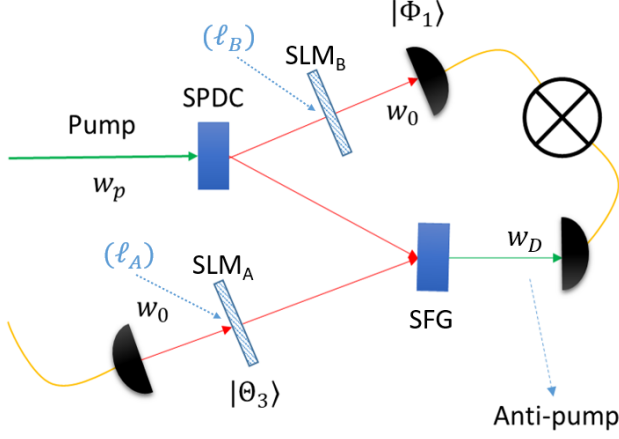


FIG. 7: **Teleportation channel scheme with optimisation parameters.** A pump photon with a waist size of  $w_p$  impinges on a nonlinear crystal, generating two photons, photon B and photon C. Photon C is transmitted to a second crystal for spontaneous parametric up-conversion (SFG) where it is absorbed with another independent photon encoded with the mode  $|\Theta_3\rangle$ , corresponding to a mode field with a waist size of  $w_0$ . We will call this independent photon, photon A. To recover the spatial information of photon A, we scan the spatial mode of photon B with spatial projections mapping onto the state  $|\Phi_1\rangle$  with a corresponding mode field that also has a waist size of  $w_0$ .  $\ell_A$  and  $\ell_B$  refer to the encoded and projected vortex states displayed on the spatial light modulators (SLMs).

modes using photons A and C, respectively. A summary of the experiment with the relevant parameters is given in Fig. S7. Here the up-conversion field radius ( $w_0$ ) is set by the detection fibre in the system.

Now supposing we want to teleport the spatial information of photon A to photon B, let the modes corresponding to each photon be expressed as

$$|\Phi_1\rangle = \int \phi(\mathbf{q}_B) |\mathbf{q}_B\rangle d^2q_B, \quad (45)$$

and

$$|\Theta_3\rangle = \int \theta(\mathbf{q}_A) |\mathbf{q}_A\rangle d^2q_A, \quad (46)$$

where  $\phi(\cdot)$  and  $\theta(\cdot)$  are the field amplitudes, respectively. The overlap probability amplitude, given the teleportation matrix presented earlier, is therefore

$$\begin{aligned} \langle \Phi_1 | \hat{T} | \Theta_3 \rangle &= \int \phi^\dagger(\mathbf{q}_B) \theta(\mathbf{q}_A) \\ &\quad \times T'(\mathbf{q}_B - \mathbf{q}_A) d^2q_B d^2q_A. \end{aligned} \quad (47)$$

Since the weighting function of the channel matrix depends only on the relative momenta, we can simplify the integral

$$\langle \Phi_1 | \hat{T} | \Theta_3 \rangle = \int \phi^\dagger(\mathbf{q}_B) \theta'(\mathbf{q}_B) d^2q_B, \quad (48)$$

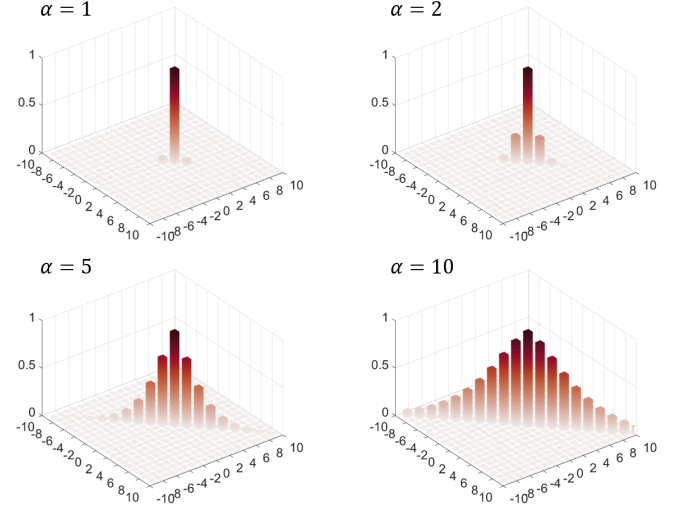


FIG. 8: **Modal spectrum from measurements of photon B for the encoded states of photon A.** Vortex modes for various  $\alpha = w_p/w_0$  with a fixed  $\beta = w_p/w_c = 1$  were used as the teleported states. The modal spectrum shows non-zero probabilities for  $\ell_1 = \ell_3$ . Moreover, the spectrum becomes wider with increasing  $\alpha$ . This means that the teleported and detected mode sizes must be significantly smaller than the SPDC mode to see a wider spectrum.

where  $\theta'(\mathbf{q}) = \theta * T$  is a simple convolution.

For the numerical calculation, vortex modes will be considered, which are basis modes with orbital angular momentum (OAM or  $\ell$ ), i.e.  $|\Phi_1\rangle, |\Theta_3\rangle \in \{|\ell\rangle, \ell \in \mathcal{Z}\}$ .

Photon A is then encoded with the vortex modes, using phase-only modulation:

$$|\ell\rangle = \int G(\mathbf{q}; w_0) \exp(i\ell\phi_q) |\mathbf{q}\rangle d^2q, \quad (49)$$

where  $\ell$  is the topological charge of the mode,  $\phi$  is the azimuth coordinate and  $G(\mathbf{q}; w_0)$  is a Gaussian mode with a transverse waist of  $w_0$  at the crystal plane. The photon B is projected onto these vortex modes. To ascertain the best experimental settings for measuring a large spectrum of OAM modes through the channel, the parameters  $\alpha = w_p/w_0$  and  $\beta = w_p/w_D$  are considered.

In Fig. 8, the conditional probabilities

$$P_{\ell_B, \ell_A}(\alpha) = |\langle \ell_B | \hat{T} | \ell_A \rangle|^2, \quad (50)$$

are presented for various  $\alpha$  values with a fixed  $\beta = 1$  ( $w_D = w_p$ ), i.e. the anti-pump and SPDC pump modes are the same size. Here, larger values of  $\alpha$  widen the modal spectrum, which can be seen in Fig. 9(a) where only the diagonals are extracted. Therefore, larger values of  $\alpha$  increases the dimensionality of the system. The dimensions can be quantitatively measured using the Schmidt number

$$K(\alpha) = \frac{1}{\sum_{\ell} P_{\ell}^2(\alpha)}, \quad (51)$$

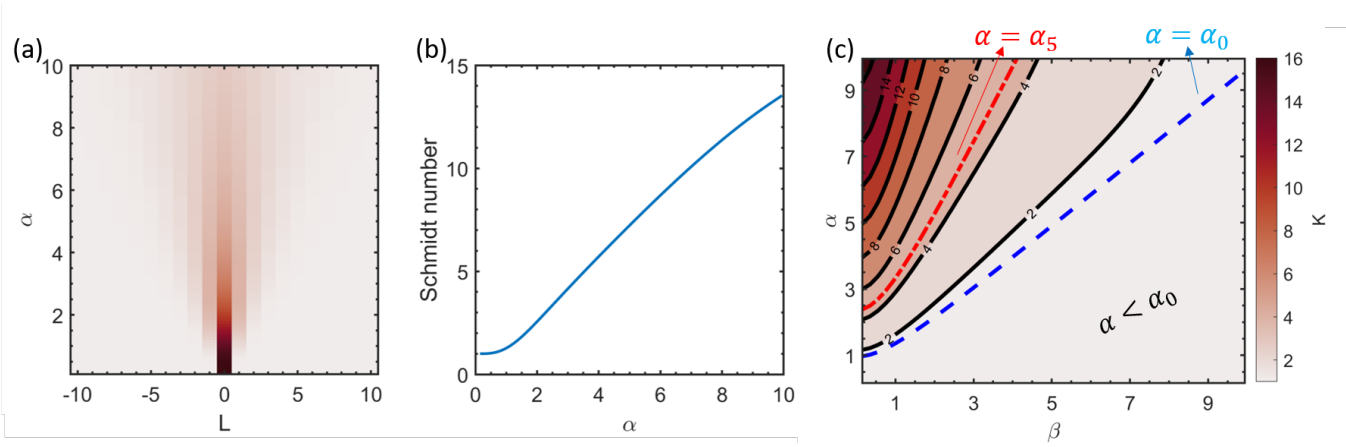


FIG. 9: **Density plot of the spiral spectrum as a function of  $\alpha$  and  $\ell = L$ .** Only the diagonal is shown. The dimensionality ( $K$ ), measured from the Schmidt number vs  $\alpha = w_p/w_0$  with a fixed  $\beta = w_p/w_c = 1$ . Contour plot of the dimensionality ( $K$ ) as a function of  $\beta$  and  $\alpha$ . For higher dimensionality we need a small  $\beta < 1$  and large  $\alpha$ . In the experiment this means that we must ensure that the SPDC is smaller than the anti-pump mode while significantly larger than the detection modes. The blue single dash line corresponds to the minimum  $\alpha = \alpha_0$  for teleporting a spatial mode through the setup. The red double dashed line corresponds to the minimum  $\alpha = \alpha_5$  for teleporting OAM modes with  $\ell = [-5, 5] = [-2, 2]$  giving access to no more than  $K = 5$  dimensions.

where  $P_\ell(\alpha) = |\langle \ell | \hat{T} | \ell \rangle|^2$ .

The subsequent dimensionality  $K$  is given in Fig. 9(b) as a function of  $\alpha$ . It can be seen that an increase in the dimensionality of the modes requires a large  $\alpha$  or  $w_p > w_0$ . Figure 9(c) further shows the dimensionality as a function of  $\alpha$  and  $\beta$  in a contour plot. Here, a larger value for  $\beta$  yields a larger accessible dimensionality. Consequently, for detection of a dimensionality larger than two,

$$\alpha > \alpha_0 = \frac{n_A}{n_B} \sqrt{\beta + 1}. \quad (52)$$

The blue dashed line in Fig. 9(c) corresponds to  $\alpha_0$  for various  $\beta$  values. Indeed the dimensionality below this region is less than  $K=2$ . This is due to  $w_0$  corresponding to the Gaussian argument of the vortex modes and not the optimal mode size of the generated or detected vortex mode.

To detect higher dimensional states, the scaling of higher order modes must be taken into account. Therefore, by noting that OAM basis modes increase in size by a factor of  $M_\ell = \sqrt{|\ell| + 1}$  the relation  $\alpha > \alpha_\ell$  where  $\alpha_\ell = \sqrt{\beta + 1} M_\ell$  should be satisfied. This observation is illustrated for  $\alpha_5$  as the red dashed line in Fig. 9(c). Below this line, only states with less than  $K = 5$  dimensions are accessible. Accordingly,  $\alpha_\ell$  sets a restriction on the upper limit of the dimensions accessible with the teleportation system.

Varying these parameters in the experimental setup, we obtained the spiral bandwidths shown in Fig. 1 (c-e) of the main text for the experimental parameters given in Table I and marked on the contour plot in Fig. 1 (b) of the text.

It follows that a large  $\beta$  generates a very small bandwidth with only one OAM mode discernibly present in

Fig. 1 (main text)	$\beta$	$\alpha$
c	4.1	2.7
d	1.1	2.7
e	1.1	4.1

TABLE I: **Experimentally tested parameters.** Parameters values used experimentally to test the numerically simulated dimensionality trends.

(c). Changing  $\beta$  to be near 1 showed more modes present (see Fig. 1 (d) in main text). Further optimising the parameters with an increase in  $\alpha$  then allowed an additional increase in the spiral bandwidth.

## VI. PROCRUSTEAN FILTERING

Experimental factors required compensation when evaluating the teleported results in the OAM basis and required the application of correction to the detected coincidences. These were the result of a convolution of corrections resulting from a non-flat spiral bandwidth from the SPDC photons [53, 54], variation in the overlap of the DC 806 nm photons and the 1565 nm photons in the SFG process (as shown by the teleportation operator) and the fixed-size Gaussian filter resulting from detection with a single mode fiber [55]. Supplementary Figure 10(a) shows the spiral bandwidth (at 2 minute integration time per point) resulting from these factors with a (i) density plot and the associated (ii) correlated modes diagonal as well as a (iii) 3D-representation, highlighting the non-flat spectrum.

As a flat spiral bandwidth is preferable for unbiased teleportation of states, the modal weights were equalised

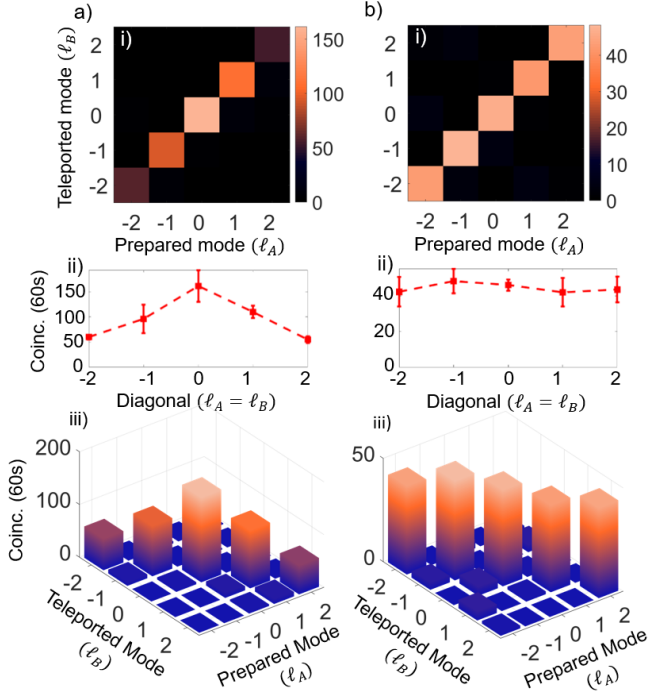


FIG. 10: **Procrustean filtering of the OAM modes.** Unflattened (a) and flattened (b) spiral bandwidths by decreasing the grating depth for lower  $\ell$ -values. Here (i) gives the density plot, (ii) shows the diagonal of (i) and (iii) renders the data in 3D where the diagonal values are highlighted in a green colormap.

by a mode-specific decrease of the grating depth for the holograms, allowing one to implement Procrustean filtering [56–58] and thus sacrificing signal for the smaller  $|\ell|$ -values.

Supplementary Figure 10(b) shows the result of implementing an  $\ell$ -dependent grating depth compensation. Here it can be seen that the detected weights across the 5 OAM modes were flattened to within the experimental uncertainties, with a small increase in the  $\ell = 1$  mode due to laser fluctuation. This, however, does come at the cost of a smaller signal-to-noise ratio as is demonstrated in the density and 3D-plots given in (b)(i) and (b)(iii) respectively (maximum coincidences are less by about a third). Supplementary Figures 10 (ii) show the diagonals for clearer comparison of the modal weights.

## VII. BACKGROUND SUBTRACTION

Due to the low efficiencies in the up-conversion process, a low signal to noise ratio was an experimental factor. An additional mode-dependent noise was also observed as a result of two photon absorption occurring for lower  $\ell$ -values as the 1565 nm pump power density is higher. As a result, the visibilities and fidelities of the states are decreased. Here, reducing the window for which the coincidences were detected aided to reduce the noise at the

OAM Superposition	Raw Visibility	B. Sub. Visibility
$\frac{1}{\sqrt{2}}( 1\rangle +  -1\rangle)$	0.85	0.96
$\frac{1}{\sqrt{2}}( 2\rangle +  -2\rangle)$	0.83	0.96
$\frac{1}{\sqrt{2}}( 3\rangle +  -3\rangle)$	0.79	0.97
$\frac{1}{\sqrt{2}}( 4\rangle +  -4\rangle)$	0.65	0.94
3D Tomography	Raw Fidelity	B. Sub. Fidelity
$\frac{1}{\sqrt{3}}( -1\rangle +  0\rangle +  1\rangle)$	0.66	0.75
2D OAM Superposition	Raw Similarity	B. Sub. Similarity
$ \varphi_1\rangle$	0.987	0.989
$ \varphi_2\rangle$	0.981	0.976
$ \varphi_3\rangle$	0.986	0.989
3D OAM Superposition	Raw Similarity	B. Sub. Similarity
$ \varphi_4\rangle$	0.978	0.970
4D OAM Superposition	Raw Similarity	B. Sub. Similarity
$ \varphi_5\rangle$	0.989	0.983
3D HG Superposition	Raw Similarity	B. Sub. Similarity
$ \gamma_1\rangle$	0.996	0.995
4D HG Superposition	Raw Similarity	B. Sub. Similarity
$ \gamma_2\rangle$	0.985	0.985
9D HG Superposition	Raw Similarity	B. Sub. Similarity
$ \gamma_3\rangle$	0.899	0.907

TABLE II: **Results summary of background subtracted and raw data.** Experimental visibilities, fidelities and similarities calculated for the teleportation channel and teleported states comparing raw and background subtracted (B. Sub.) outcomes. Abbreviated states are  $|\varphi_1\rangle = \frac{1}{\sqrt{2}}[|0\rangle + |-1\rangle]$ ,  $|\varphi_2\rangle = \frac{1}{\sqrt{2}}[|-1\rangle + |1\rangle]$ ,  $|\varphi_3\rangle = \frac{1}{\sqrt{2}}[|0\rangle - |1\rangle]$ ,  $|\varphi_4\rangle = \frac{1}{\sqrt{3}}[|-2\rangle + |0\rangle + |2\rangle]$ ,  $|\gamma_1\rangle = \frac{1}{\sqrt{3}}[|HG_{1,0}\rangle + |HG_{1,1}\rangle + |HG_{0,1}\rangle]$ ,  $|\varphi_5\rangle = \frac{1}{\sqrt{4}}[|-3\rangle - i|-1\rangle + |1\rangle + i|3\rangle]$ ,  $|\gamma_2\rangle = \frac{1}{\sqrt{4}}[|HG_{0,0}\rangle + |HG_{1,0}\rangle + |HG_{1,1}\rangle + |HG_{0,1}\rangle]$  and  $|\gamma_3\rangle = \frac{1}{\sqrt{9}}[|HG_{0,0}\rangle + |HG_{2,0}\rangle + |HG_{0,2}\rangle + |HG_{2,2}\rangle + |HG_{4,0}\rangle + |HG_{0,4}\rangle + |HG_{4,2}\rangle + |HG_{2,4}\rangle + |HG_{4,4}\rangle]$ , as given in the main text.

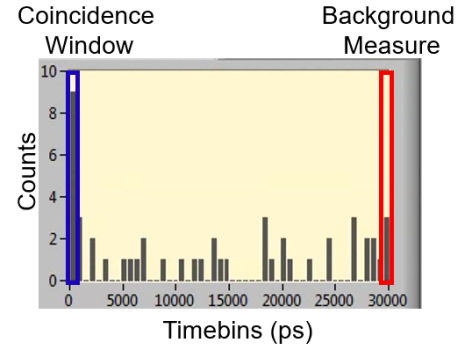


FIG. 11: **Illustration of background measurement.** Histogram showing the arm delays with the coincidence windows, demonstrating the measured background values for noise correction.

cost of some signal. Another method which was employed was to measure the detected 'coincidences' far away from the actual arrival window of the entangled photons. That measurement was then taken as the background noise of the system and subtracted from the actual measured coincidences. This is illustrated in the histogram shown in



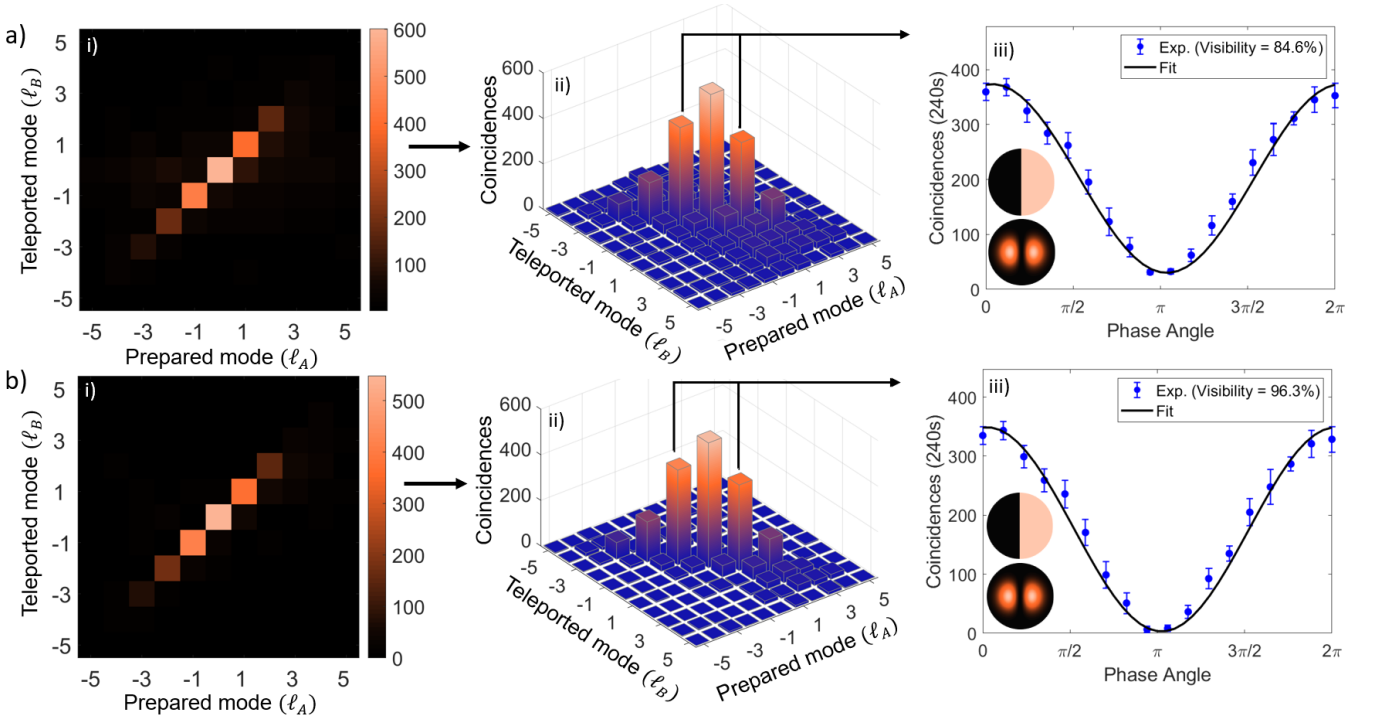


FIG. 12: **Effects of applying noise correction to the results.** Plots showing the (a) raw measured coincidences and (b) coincidences corrected by subtracting the background measured in an uncorrelated timebin for the (i) spiral bandwidth with a (ii) 3D rendering and (iii) the visibility measurable for rotating the projected state for the  $\ell = \pm 1$  teleported state.

Suppl. Fig. 11 of the measured coincidences vs. time delay for the signals received from Alice and Bob's arm. Here the blue rectangle highlights the coincidences being detected while the red highlights the values taken to be the background or noise signal.

These measured coincidence values were consequently in the same length time bin (0.5ns) with the time delay being 30 ns outside of the actual coincidence window (20 times away from the actual coincidence window). By subtracting the noise signal, the actual coincidences from the teleportation process was determined. The results of this subtraction is then showcased in Suppl. Fig. 12 for the spiral bandwidth and visibility from a superposition OAM state of  $\ell = \pm 1$ . Here, Suppl. Fig. 12(a) shows the raw measured results, while (b) illustrates the effects of subtracting the measured noise from the coincidences as described in Suppl. Fig. 11. (i) shows the spiral bandwidth ranging from  $\ell = -5$  to  $\ell = 5$  with a 5 minute integration time per projection measurement. (ii) gives the 3D rendering of the measurements so that the noise can be easily seen. (iii) then gives the  $\ell = \pm 1$  superposition state where the projection state was rotated by adjusting the intermodal phase from  $\theta = [0, 2\pi]$ . In all cases a clear improvement in the measured states can be seen with particular attention to the increase in visibility of Suppl. Fig. 12 (b, iii) from (a, iii), reaching almost a perfect fidelity of the teleported state.

A summary of the difference in visibilities for rotations of the different projected modes shown in Fig. 3(a) of the main text is further provided in Table II, along with the

other results given throughout the paper.

## VIII. PROCESS EFFICIENCIES

Since the teleportation protocol presented here, is based on single photon pairs, the efficiency of the nonlinear process is required to be very small. Under such conditions, the complete state produced by SPDC can be represented by

$$|\psi_{\text{SPDC}}\rangle \approx |\text{vac}\rangle + |\psi_{BC}\rangle \sigma + O\{\sigma^2\}, \quad (53)$$

where  $\sigma \ll 1$  is the nonlinear coefficient which is determined by

$$\sigma = \chi^{(2)} \sqrt{\frac{\hbar \omega_p \omega_B \omega_C}{8 \epsilon_0 c^3 n_p n_B n_C}} \frac{F_0}{A_p}. \quad (54)$$

Here,  $\chi^{(2)}$  is the second-order nonlinear susceptibility coefficient of the nonlinear material for a given phase-matching condition, the subscript  $p$  refers to the pump,  $F_0/A_p$  is the number of pump photons per second per area or flux rate (photons/s/m<sup>2</sup>),  $n$  refers to the respective refractive indices,  $\omega$  refers to the respective central angular frequencies,  $c$  is the speed of light, and  $\epsilon_0$  is the electrical permittivity of free space (see Refs. [59, 60] for more details on upconversion efficiency using spatial modes).

- 
- [1] C. H. Bennett, G. Brassard, C. Crépeau, R. Jozsa, A. Peres, and W. K. Wootters, “Teleporting an unknown quantum state via dual classical and einstein-podolsky-rosen channels,” *Physical review letters*, vol. 70, no. 13, p. 1895, 1993.
  - [2] N. Gisin, G. Ribordy, W. Tittel, and H. Zbinden, “Quantum cryptography,” *Rev. Mod. Phys.*, vol. 74, pp. 145–195, Mar 2002.
  - [3] H. J. Kimble, “The quantum internet,” *Nature*, vol. 453, no. 7198, pp. 1023–1030, 2008.
  - [4] J. T. Barreiro, T.-C. Wei, and P. G. Kwiat, “Beating the channel capacity limit for linear photonic superdense coding,” *Nature physics*, vol. 4, no. 4, pp. 282–286, 2008.
  - [5] F. Bouchard, R. Fickler, R. W. Boyd, and E. Karimi, “High-dimensional quantum cloning and applications to quantum hacking,” *Science advances*, vol. 3, no. 2, p. e1601915, 2017.
  - [6] S. Ecker, F. Bouchard, L. Bulla, F. Brandt, O. Kohout, F. Steinlechner, R. Fickler, M. Malik, Y. Guryanova, R. Ursin, *et al.*, “Overcoming noise in entanglement distribution,” *Physical Review X*, vol. 9, no. 4, p. 041042, 2019.
  - [7] J. Calsamiglia, “Generalized measurements by linear elements,” *Physical Review A*, vol. 65, no. 3, p. 030301, 2002.
  - [8] S. Molotkov, “Quantum teleportation of a single-photon wave packet,” *Physics Letters A*, vol. 245, no. 5, pp. 339–344, 1998.
  - [9] Y. Zhang, M. Agnew, T. Roger, F. S. Roux, T. Konrad, D. Faccio, J. Leach, and A. Forbes, “Simultaneous entanglement swapping of multiple orbital angular momentum states of light,” *Nature Communications*, vol. 8, no. 1, p. 632, 2017.
  - [10] S. Liu, Y. Lou, and J. Jing, “Orbital angular momentum multiplexed deterministic all-optical quantum teleportation,” *Nature communications*, vol. 11, no. 1, pp. 1–8, 2020.
  - [11] X.-L. Wang, X.-D. Cai, Z.-E. Su, M.-C. Chen, D. Wu, L. Li, N.-L. Liu, C.-Y. Lu, and J.-W. Pan, “Quantum teleportation of multiple degrees of freedom of a single photon,” *Nature*, vol. 518, no. 7540, pp. 516–519, 2015.
  - [12] Y.-H. Luo, H.-S. Zhong, M. Erhard, X.-L. Wang, L.-C. Peng, M. Krenn, X. Jiang, L. Li, N.-L. Liu, C.-Y. Lu, *et al.*, “Quantum teleportation in high dimensions,” *Physical review letters*, vol. 123, no. 7, p. 070505, 2019.
  - [13] X.-M. Hu, C. Zhang, B.-H. Liu, Y. Cai, X.-J. Ye, Y. Guo, W.-B. Xing, C.-X. Huang, Y.-F. Huang, C.-F. Li, and G.-C. Guo, “Experimental high-dimensional quantum teleportation,” *Phys. Rev. Lett.*, vol. 125, p. 230501, Dec 2020.
  - [14] M. A. Nielsen and I. Chuang, “Quantum computation and quantum information,” 2002.
  - [15] M. M. Wilde, *Quantum information theory*. Cambridge University Press, 2013.
  - [16] C. Weedbrook, S. Pirandola, R. García-Patrón, N. J. Cerf, T. C. Ralph, J. H. Shapiro, and S. Lloyd, “Gaussian quantum information,” *Reviews of Modern Physics*, vol. 84, no. 2, p. 621, 2012.
  - [17] R. Raussendorf and H. J. Briegel, “A one-way quantum computer,” *Physical Review Letters*, vol. 86, no. 22, p. 5188, 2001.
  - [18] D. Gottesman and I. L. Chuang, “Demonstrating the viability of universal quantum computation using teleportation and single-qubit operations,” *Nature*, vol. 402, no. 6760, pp. 390–393, 1999.
  - [19] M. Barrett, J. Chiaverini, T. Schaetz, J. Britton, W. Itano, J. Jost, E. Knill, C. Langer, D. Leibfried, R. Ozeri, *et al.*, “Deterministic quantum teleportation of atomic qubits,” *Nature*, vol. 429, no. 6993, pp. 737–739, 2004.
  - [20] M. Riebe, H. Häffner, C. Roos, W. Hänsel, J. Benhelm, G. Lancaster, T. Körber, C. Becher, F. Schmidt-Kaler, D. James, *et al.*, “Deterministic quantum teleportation with atoms,” *Nature*, vol. 429, no. 6993, pp. 734–737, 2004.
  - [21] H.-J. Briegel, W. Dür, J. I. Cirac, and P. Zoller, “Quantum repeaters: The role of imperfect local operations in quantum communication,” *Phys. Rev. Lett.*, vol. 81, pp. 5932–5935, Dec 1998.
  - [22] I. Marcikic, H. De Riedmatten, W. Tittel, H. Zbinden, and N. Gisin, “Long-distance teleportation of qubits at telecommunication wavelengths,” *Nature*, vol. 421, no. 6922, pp. 509–513, 2003.
  - [23] J.-G. Ren, P. Xu, H.-L. Yong, L. Zhang, S.-K. Liao, J. Yin, W.-Y. Liu, W.-Q. Cai, M. Yang, L. Li, *et al.*, “Ground-to-satellite quantum teleportation,” *Nature*, vol. 549, no. 7670, pp. 70–73, 2017.
  - [24] D. Bouwmeester, J.-W. Pan, K. Mattle, M. Eibl, H. Weinfurter, and A. Zeilinger, “Experimental quantum teleportation,” *Nature*, vol. 390, no. 6660, pp. 575–579, 1997.
  - [25] J. Yin, Y. Cao, Y.-H. Li, S.-K. Liao, L. Zhang, J.-G. Ren, W.-Q. Cai, W.-Y. Liu, B. Li, H. Dai, G.-B. Li, Q.-M. Lu, Y.-H. Gong, Y. Xu, S.-L. Li, F.-Z. Li, Y.-Y. Yin, Z.-Q. Jiang, M. Li, J.-J. Jia, G. Ren, D. He, Y.-L. Zhou, X.-X. Zhang, N. Wang, X. Chang, Z.-C. Zhu, N.-L. Liu, Y.-A. Chen, C.-Y. Lu, R. Shu, C.-Z. Peng, J.-Y. Wang, and J.-W. Pan, “Satellite-based entanglement distribution over 1200 kilometers,” *Science*, vol. 356, no. 6343, pp. 1140–1144, 2017.
  - [26] X.-L. Wang, L.-K. Chen, W. Li, H.-L. Huang, C. Liu, C. Chen, Y.-H. Luo, Z.-E. Su, D. Wu, Z.-D. Li, *et al.*, “Experimental ten-photon entanglement,” *Physical review letters*, vol. 117, no. 21, p. 210502, 2016.
  - [27] A. Furusawa, J. L. Sørensen, S. L. Braunstein, C. A. Fuchs, H. J. Kimble, and E. S. Polzik, “Unconditional quantum teleportation,” *Science*, vol. 282, no. 5389, pp. 706–709, 1998.
  - [28] N. Takei, H. Yonezawa, T. Aoki, and A. Furusawa, “High-fidelity teleportation beyond the no-cloning limit and entanglement swapping for continuous variables,” *Physical review letters*, vol. 94, no. 22, p. 220502, 2005.
  - [29] H. Yonezawa, S. L. Braunstein, and A. Furusawa, “Experimental demonstration of quantum teleportation of broadband squeezing,” *Physical review letters*, vol. 99, no. 11, p. 110503, 2007.
  - [30] N. Lee, H. Benichi, Y. Takeno, S. Takeda, J. Webb, E. Huntington, and A. Furusawa, “Teleportation of nonclassical wave packets of light,” *Science*, vol. 332, no. 6027, pp. 330–333, 2011.
  - [31] M. A. Nielsen, E. Knill, and R. Laflamme, “Complete quantum teleportation using nuclear magnetic resonance,” *Nature*, vol. 396, no. 6706, pp. 52–55, 1998.

- [32] J. F. Sherson, H. Krauter, R. K. Olsson, B. Julsgaard, K. Hammerer, I. Cirac, and E. S. Polzik, “Quantum teleportation between light and matter,” *Nature*, vol. 443, no. 7111, pp. 557–560, 2006.
- [33] S. Olmschenk, D. Matsukevich, P. Maunz, D. Hayes, L.-M. Duan, and C. Monroe, “Quantum teleportation between distant matter qubits,” *Science*, vol. 323, no. 5913, pp. 486–489, 2009.
- [34] A. Mair, A. Vaziri, G. Weihs, and A. Zeilinger, “Entanglement of the orbital angular momentum states of photons,” *Nature*, vol. 412, no. 6844, pp. 313–316, 2001.
- [35] G. Molina-Terriza, J. P. Torres, and L. Torner, “Twisted photons,” *Nat Phys*, vol. 3, no. 5, pp. 305–310, 2007.
- [36] D. Cozzolino, B. Da Lio, D. Bacco, and L. K. Oxenløwe, “High-dimensional quantum communication: benefits, progress, and future challenges,” *Advanced Quantum Technologies*, vol. 2, no. 12, p. 1900038, 2019.
- [37] A. Forbes and I. Nape, “Quantum mechanics with patterns of light: progress in high dimensional and multi-dimensional entanglement with structured light,” *AVS Quantum Science*, vol. 1, no. 1, p. 011701, 2019.
- [38] M. Erhard, R. Fickler, M. Krenn, and A. Zeilinger, “Twisted photons: new quantum perspectives in high dimensions,” *Light: Science & Applications*, vol. 7, no. 3, pp. 17146–17146, 2018.
- [39] W. Son, J. Lee, M. Kim, and Y.-J. Park, “Conclusive teleportation of a d-dimensional unknown state,” *Physical Review A*, vol. 64, no. 6, p. 064304, 2001.
- [40] R. F. Werner, “All teleportation and dense coding schemes,” *Journal of Physics A: Mathematical and General*, vol. 34, no. 35, p. 7081, 2001.
- [41] S. K. Goyal, P. E. Boukama-Dzoussi, S. Ghosh, F. S. Roux, and T. Konrad, “Qudit-teleportation for photons with linear optics,” *Scientific Reports*, vol. 4, no. 1, p. 4543, 2014.
- [42] A. A. Melnikov, H. P. Nautrup, M. Krenn, V. Dunjko, M. Tiersch, A. Zeilinger, and H. J. Briegel, “Active learning machine learns to create new quantum experiments,” *Proceedings of the National Academy of Sciences*, vol. 115, no. 6, pp. 1221–1226, 2018.
- [43] S. P. Walborn, C. Monken, S. Pádua, and P. S. Ribeiro, “Spatial correlations in parametric down-conversion,” *Physics Reports*, vol. 495, no. 4-5, pp. 87–139, 2010.
- [44] T. S. Humble, “Spectral and spread-spectral teleportation,” *Physical Review A*, vol. 81, no. 6, p. 062339, 2010.
- [45] Y.-H. Kim, S. P. Kulik, and Y. Shih, “Quantum teleportation of a polarization state with a complete bell state measurement,” *Phys. Rev. Lett.*, vol. 86, pp. 1370–1373, Feb 2001.
- [46] Z.-Y. Zhou, Y. Li, D.-S. Ding, W. Zhang, S. Shi, B.-S. Shi, and G.-C. Guo, “Orbital angular momentum photonic quantum interface,” *Light: Science & Applications*, vol. 5, no. 1, pp. e16019–e16019, 2016.
- [47] M. Jiang, S. Luo, and S. Fu, “Channel-state duality,” *Physical Review A*, vol. 87, no. 2, p. 022310, 2013.
- [48] I. Nape, V. Rodríguez-Fajardo, F. Zhu, H.-C. Huang, J. Leach, and A. Forbes, “Measuring dimensionality and purity of high-dimensional entangled states,” *Nature Communications*, vol. 12, no. 1, pp. 1–8, 2021.
- [49] C. H. Bennett, D. P. DiVincenzo, P. W. Shor, J. A. Smolin, B. M. Terhal, and W. K. Wootters, “Remote state preparation,” *Phys. Rev. Lett.*, vol. 87, p. 077902, Jul 2001.
- [50] B. Collins and P. Śniady, “Integration with respect to the haar measure on unitary, orthogonal and symplectic group,” *Communications in Mathematical Physics*, vol. 264, no. 3, pp. 773–795, 2006.
- [51] S. Molotkov, “Experimental scheme for quantum teleportation of a single-photon packet,” *arXiv preprint quant-ph/9807013*, 1998.
- [52] M. Erhard, M. Krenn, and A. Zeilinger, “Advances in high-dimensional quantum entanglement,” *Nature Reviews Physics*, vol. 2, no. 7, pp. 365–381, 2020.
- [53] C. Law and J. Eberly, “Analysis and interpretation of high transverse entanglement in optical parametric down conversion,” *Phys Rev Lett*, vol. 92, no. 12, p. 127903, 2004.
- [54] J. Torres, A. Alexandrescu, and L. Torner, “Quantum spiral bandwidth of entangled two-photon states,” *Phys Rev A*, vol. 68, no. 5, p. 050301, 2003.
- [55] F. S. Roux and Y. Zhang, “Projective measurements in quantum and classical optical systems,” *Physical Review A*, vol. 90, no. 3, p. 033835, 2014.
- [56] A. Vaziri, J.-W. Pan, T. Jennewein, G. Weihs, and A. Zeilinger, “Concentration of higher dimensional entanglement: qutrits of photon orbital angular momentum,” *Physical review letters*, vol. 91, no. 22, p. 227902, 2003.
- [57] A. C. Dada, J. Leach, G. S. Buller, M. J. Padgett, and E. Andersson, “Experimental high-dimensional two-photon entanglement and violations of generalized bell inequalities,” *Nat Phys*, vol. 7, no. 9, p. 677, 2011.
- [58] C. H. Bennett, H. J. Bernstein, S. Popescu, and B. Schumacher, “Concentrating partial entanglement by local operations,” *Physical Review A*, vol. 53, no. 4, p. 2046, 1996.
- [59] G. Boyd and D. Kleinman, “Parametric interaction of focused gaussian light beams,” *Journal of Applied Physics*, vol. 39, no. 8, pp. 3597–3639, 1968.
- [60] B. Sephton, A. Vallés, F. Steinlechner, T. Konrad, J. P. Torres, F. S. Roux, and A. Forbes, “Spatial mode detection by frequency upconversion,” *Opt. Lett.*, vol. 44, pp. 586–589, Feb 2019.